PLOS Genetics

RESEARCH ARTICLE

RAB23 loss-of-function mutation causes context-dependent ciliopathy in Carpenter syndrome

Wan Ying Leong[2☯], Wai Lam Tung[1], Andrew O. M. Wilkie[3], Catherine Hong Huan Hor[1,2☯*]

1 Department of Chemistry, Faculty of Science, Hong Kong Baptist University, Kowloon, Hong Kong,
2 Neuroscience Academic Clinical Programme, Duke-NUS Medical School, Singapore, Singapore,
3 MRC Weatherall Institute of Molecular Medicine, University of Oxford, John Radcliffe Hospital, Oxford, United Kingdom

☯ These authors contributed equally to this work, co-first author.
* catherinehor@hkbu.edu.hk

Abstract

The primary cilium is a signal transduction organelle whose dysfunction clinically causes ciliopathies in humans. RAB23 is a small GTPase known to regulate the Hedgehog signalling pathway and ciliary trafficking. Mutations of *RAB23* in humans lead to Carpenter syndrome (CS), an autosomal recessive disorder clinically characterized by craniosynostosis, polysyndactyly, skeletal defects, obesity, and intellectual disability. Although the clinical features of CS bear some resemblance to those of ciliopathies, the exact relationship between the pathological manifestations of CS and the ciliary function of *RAB23* remains ambiguous. Besides, the *in vivo* ciliary functions of *RAB23* remain poorly characterised. Here, we demonstrate *in vivo* and *in vitro Rab23* loss-of-function mutants modelling CS, including *Rab23* conditional knockout (CKO) mouse mutants, CS patient-derived induced pluripotent stem cells (iPSCs), and zebrafish morphants. The *Rab23*-CKO mutants exhibit multiple developmental and phenotypical traits recapitulating the clinical features of human ciliopathies and CS, indicating a causal link between the loss of *Rab23* and ciliopathy. In line with the ciliopathy-like phenotypes, all three different vertebrate mutant models consistently show a perturbation of primary cilia formation, intriguingly, in a context-dependent manner. *Rab23*-CKO mutants reveal cell-type specific ciliary abnormalities in chondrocytes, mouse embryonic fibroblasts, neural progenitor cells and neocortical neurons, but not in epithelial cells, cerebellar granule cells and hippocampus neurons. A profound reduction in ciliation frequency was observed specifically in neurons differentiated from CS patient iPSCs, whereas the patients' fibroblasts, iPSCs and neural progenitor cells maintained normal ciliation percentages but shortened cilia length. Furthermore, *Rab23*-KO neural progenitor cells show perturbed ciliation and desensitized to primary cilium-dependent activation of the Hedgehog signaling pathway. Collectively, these findings indicate that the absence of *RAB23* causes dysfunctional primary cilia in a cell-type distinctive manner, which underlies the pathological

Citation: Leong WY, Tung WL, Wilkie AOM, Hor CHH (2025) *RAB23* loss-of-function mutation causes context-dependent ciliopathy in Carpenter syndrome. PLoS Genet 21(8): e1011611. https://doi.org/10.1371/journal.pgen.1011611

Editor: Susan K. Dutcher, Washington University School of Medicine, UNITED STATES OF AMERICA

Received: February 10, 2025

Accepted: July 23, 2025

Published: August 18, 2025

Data availability statement: All data is provided in the manuscript and Supporting Information.

Funding: This study was supported by Research Grants Council-Collaborative Research Fund (CRF-C2103-20GF), Hong Kong

Baptist University Seed Fund, and the National Medical Research Council–Young Individual Research Grant (NMRC/OFYIRG/0079/2018) to C.H.H. H. Work on CS in AOMW's laboratory was supported by the UKRI Medical Research Council. The funders had no role in study design, data collection and analysis, decision to publish, or preparation of the manuscript.

Competing interests: The authors have declared that no competing interests exist.

manifestations of CS. Our findings present the first *in vivo* evidence validating the unique context-specific function of *RAB23* in the primary cilium. Through the use of patient-derived iPSCs differentiated cells, we present direct evidence of primary cilia anomalies in CS, thereby confirming CS as a ciliopathy disorder.

Author summary

RAB23 mutations lead to Carpenter syndrome (CS), which manifests multiple clinical features resembling those of ciliopathies, a spectrum of disorders caused by defective primary cilia. However, the *in vivo* ciliary functions of RAB23 remain ambiguous. We established multiple *Rab23* loss-of-function mutants, including conditional knockout (CKO) mouse mutants, CS patient-derived induced pluripotent stem cells (iPSCs), and zebrafish morphants. These mutant models consistently show context-dependent primary cilia anomalies. *Rab23*-CKO mutants display profound ciliary abnormalities in neocortical neurons, but not in epithelial cells, cerebellar granule cells and hippocampus neurons. Aberrant cilia formation and shortened cilia were observed in the neurons and neural progenitor cells derived from CS patient iPSCs. Furthermore, *Rab23*-KO neural progenitor cells exhibit impeded primary cilium-dependent Hedgehog signaling pathway transduction. Our findings suggest that the cell-type distinctive dysfunctional primary cilia may underlie the pathological manifestations of CS. We present the first *in vivo* evidence validating the unique context-specific function of *RAB23* in the primary cilium. The results from patient-derived iPSCs differentiated cells reveal direct evidence of primary cilia anomalies in CS, confirming CS as a ciliopathy disorder.

Introduction

The primary cilium is a microtubule-based elongated protrusion found on the surface of numerous quiescent or differentiated mammalian cells. The primary cilium axoneme harbors a myriad of sensory and transmembrane receptors, making it a crucial signal transduction hub in cellular physiology [1–3]. In humans, dysfunction of the primary cilium results in a range of rare multisystemic congenital disorders that are collectively known as ciliopathies [4]. Notably, ciliopathy disorders often exhibit overlapping phenotypes albeit genetically distinct. For example, Bardet–Biedl (BBS) and Joubert (JBTS) syndromes are ciliopathies caused by different gene mutations but share multiple common phenotypes such as retinal degeneration, cerebellar malformation and cognitive impairment, polycystic kidneys, and polydactyly [5].

Carpenter syndrome (CS) is a pleiotropic autosomal recessive genetic disorder often reported in patients carrying biallelic pathogenic variants in *RAB23* [6–8]. The disorder is typically characterized by craniosynostosis, finger and toe deformity (such as polydactyly, brachydactyly, and syndactyly), visual and hearing impairments, short stature, obesity, and mild to severe intellectual disability. Other variable clinical presentations observed in CS patients include heart defects, molar agenesis, hypogenitalism, genu valgum and hydrocephaly [8–13]. Notably, numerous common clinical features of CS patients are overlapping with the common clinical hallmarks of ciliopathies, such as polysyndactyly, hydrocephaly, obesity, and intellectual disability. Despite these clinical similarities and recent speculations on the association between *RAB23* and ciliopathy [14], it remains unclear whether patients with CS exhibit defective primary cilia.

Rab23 is a member of the small GTPase family whose GDP-GTP exchange activity is promoted by its Guanine Nucleotide Exchange Factor (GEF) complex, composed of Inturned (Intu) and Fuzzy (Fuz) [15]. In mouse null mutant models, Rab23 was found to negatively regulate the Sonic hedgehog (Shh) signaling pathway [16]. The Shh signaling pathway is predominantly regulated in a primary cilium-dependent manner. In this process, the presence of Shh ligands induces Smoothened (Smo) to translocate to the primary cilium axoneme, which subsequently initiates the downstream signaling cascade through Gli transcription factors [17]. Although *Rab23* has been shown to mediate the ciliary localisation of Smo, Dopamine receptor 1 (D1R), and Kif17 [18–21], the roles of *Rab23* in primary cilia biogenesis and/or maintenance remain ambiguous and controversial. Independent groups have reported inconsistent results on the effect of siRNA-directed silencing of *Rab23* in mouse inner medullary collecting duct (IMCD3) cells. While Gerondopoulos et. al observed a reduced degree of ciliation, Leaf and von Zastrow reported an unperturbed extent of ciliation in *Rab23*-knockdown IMCD3 cells [15,19]. A similar discrepancy was also observed in the immortalized retinal pigmented epithelial (hTERT-RPE1) cell line. Two independent groups have reported a reduced ciliation [15,22], whereas another study observed no discernible change in the percentage of ciliation, despite using the same siRNA-mediated knockdown approach to silence *Rab23* in hTERT-RPE1 cells [20]. However, in our previous study on *Rab23*-knockout cerebellar primary granule progenitor cells culture [18], we observed a reduction in the length of primary cilia, albeit with an unperturbed rate of ciliation. Given these inconsistent observations on the effect of *Rab23* silencing on the primary cilia formation and its structural integrity, more extensive investigations are necessary to elucidate the precise functions of Rab23 within the primary cilium.

In this study, we have established novel disease models of Carpenter syndrome using transgenic mice and human induced pluripotent stem cells (iPSCs) reprogrammed from biopsies of Carpenter syndrome patients. Strikingly, both the global gene knockout (KO) mutants (actin-Cre), and neural progenitor cells (NPCs)-specific knockout mutants of *Rab23* display a range of developmental and phenotypic abnormalities that largely resemble the clinical features observed in Carpenter syndrome and ciliopathy patients. In these mutants, a significantly reduced number of primary cilia were observed in the cerebral neocortical neurons, NPCs, and mouse embryonic fibroblasts (MEFs), suggesting that Rab23 plays important ciliary functions in the neocortical neurons, NPCs, and MEFs. Intriguingly, the frequency of ciliated cells appeared largely unchanged in other brain regions such as the hippocampus neurons and granule precursor cells in the cerebellum, or in other non-neuronal cell types such as the epithelial cells and chondrocytes. However, *Rab23*-KO NPCs, cortical neurons, and chondrocytes show shortened cilia length. In *rab23*-silenced zebrafish morphant (*rab23* MO), the frequency of ciliation in the neural progenitor cells was predominantly perturbed in the rostral neural tube but not in other regions such as the more caudally located spinal cord neural tube nor the pronephric duct. Consistent with the evidence from mouse and zebrafish mutant models, variable extents of primary cilia anomalies were also observed in Carpenter syndrome patients' iPSCs, fibroblasts, human neural progenitor cells, and neurons differentiated from iPSCs.

Collectively, our findings demonstrate that primary cilium anomalies occur more predominantly in the *RAB23* loss-of-function neuronal cell types (albeit in distinct neuronal populations) and this phenomenon is consistently observed in the zebrafish morphants, transgenic KO mice, and human disease models of Carpenter syndrome patients, suggesting that the function of *RAB23* in the primary cilium is context-dependent and evolutionarily conserved. In summary, the collective results from various animal and cellular disease models indicate that tissue- and cell-type-specific dysfunctions of primary cilia could contribute to the pathological features of Carpenter syndrome, implying that Carpenter syndrome is a ciliopathy disorder. Moreover, *RAB23* appears to play crucial roles in the maintenance and/or biogenesis of primary cilia.

Results

Rab23-KO mouse disease models of Carpenter syndrome phenocopy ciliopathy

Aiming to elucidate Rab23's role in the functional integrity of the primary cilium and the consequence of its loss in the pathogenesis of Carpenter syndrome, we established mouse mutants of *Rab23.* In order to generate transgenic knockout mouse mutants of *Rab23*, *Rab23*$^{f/f}$ homozygous mice [18] were crossed with a β-actin-Cre driver line to induce global deletion of *Rab23* in the progenies (herein named actin-CKO). The first reported null mutant of *Rab23,* i.e., the ENU-induced *opb2* mouse mutant exhibited embryonic lethality at embryonic day (E) 12.5 [16]. Recent work has also reported an *opb2* mutant with an extended prenatal survival to E18.5 by breeding the mouse line into a C57BL6 strain [23]. Similar to the latter *opb2* mutant, our actin-CKO mutant was viable throughout the prenatal stage in the C57/BL6 background but died postnatally. The actin-CKO embryos at E12.5 exhibited polysyndactyly at 85.7% prevalence, (6 out of 7 actin-CKO embryos), displayed missing or abnormal eyes and morphologically aberrant posterior neural tube (Fig 1A). Furthermore, the actin-CKO embryo at E18.5 exhibited several prominent phenotypic characteristics that closely resembled those observed in individuals diagnosed with human Carpenter syndrome [6–9]. These characteristics encompass craniofacial anomalies, polysyndactyly, growth retardation, and brain deformities (Fig 1A–1D). Notably, a range of abnormal brain morphologies, varying from mild to severe (Figs 1A, 1B and S2), were observed. The milder cases displayed thinning and mis-patterning of the cerebral cortex (Fig 1B–1G), while an altered pattern of the cerebellar anlage at E18.5 was also evident (Fig 1B, indicated by red asterisks). Importantly, these abnormalities largely align with the common phenotypic features found in previously reported ciliopathy mutants. [24–26].

Furthermore, to investigate the specific neuronal functions of *Rab23*, lineage-specific deletion of *Rab23* was achieved in neural progenitor cells at approximately E10.5 using the Nestin-cre driver line (herein, referred to as Nes-CKO for the homozygous deleted mutant). Nes-CKO mutant mice displayed normal gross morphology appearances and survived into adulthood. They exhibited obesity (Fig 1K), and showed a significant enlargement of the brain ventricle (Fig 1I–1J, red asterisks). However, the morphological appearance of the cerebral cortex in the adult Nes-CKO mutants appeared relatively normal compared to the control counterpart (*Rab23*$^{f/f}$) (Fig 1H–1I).

Consistent with the observed mis-patterned cerebellar anlage in the embryonic actin-CKO mutants, abnormal cerebellar folia formation was also observed in the adult Nes-CKO mice (Fig 1B red asterisks, 1H yellow asterisks). These findings suggest that the mutant mice share several clinical characteristics reported in both Carpenter syndrome and ciliopathies, such as hydrocephaly and obesity [4,6–8,25,27,28]. Moreover, similar to the phenomenon in actin-CKO mutant, some cases of postnatal lethality have been reported in human patients, including one infant who died two hours after birth due to respiratory failure [29,30].

Taken together, the *Rab23* mutants prominently display multiple developmental features that closely resemble both Carpenter syndrome patients and individuals affected by other forms of ciliopathy. This strongly suggests that the loss of *Rab23* function leads to ciliopathy in the mouse mutants. Importantly, the *Rab23* loss-of-function mouse mutants serve as a robust disease model for Carpenter syndrome, as they successfully recapitulate numerous clinical characteristics observed in human patients. These mutant mice provide valuable animal platforms that will facilitate comprehensive investigations into the underlying disease mechanisms of Carpenter syndrome.

Rab23 exerts a cell-type specific function in maintaining proper primary cilium formation

Given that the aforementioned features can be found in various ciliopathy disorders [24,31–33], as well as Carpenter syndrome [7,8,29,34], our mouse model data implicates a potential mechanistic association between Carpenter syndrome and ciliopathies. Considering the apparent phenotypic correlation with ciliopathies, we investigate whether the deletion of *Rab23* would disrupt primary cilium formation and/or affect its structural integrity. To visualize primary cilia in various cell types, including epithelial cells, chondrocytes, embryonic fibroblasts, neuronal progenitors, granule cell precursors

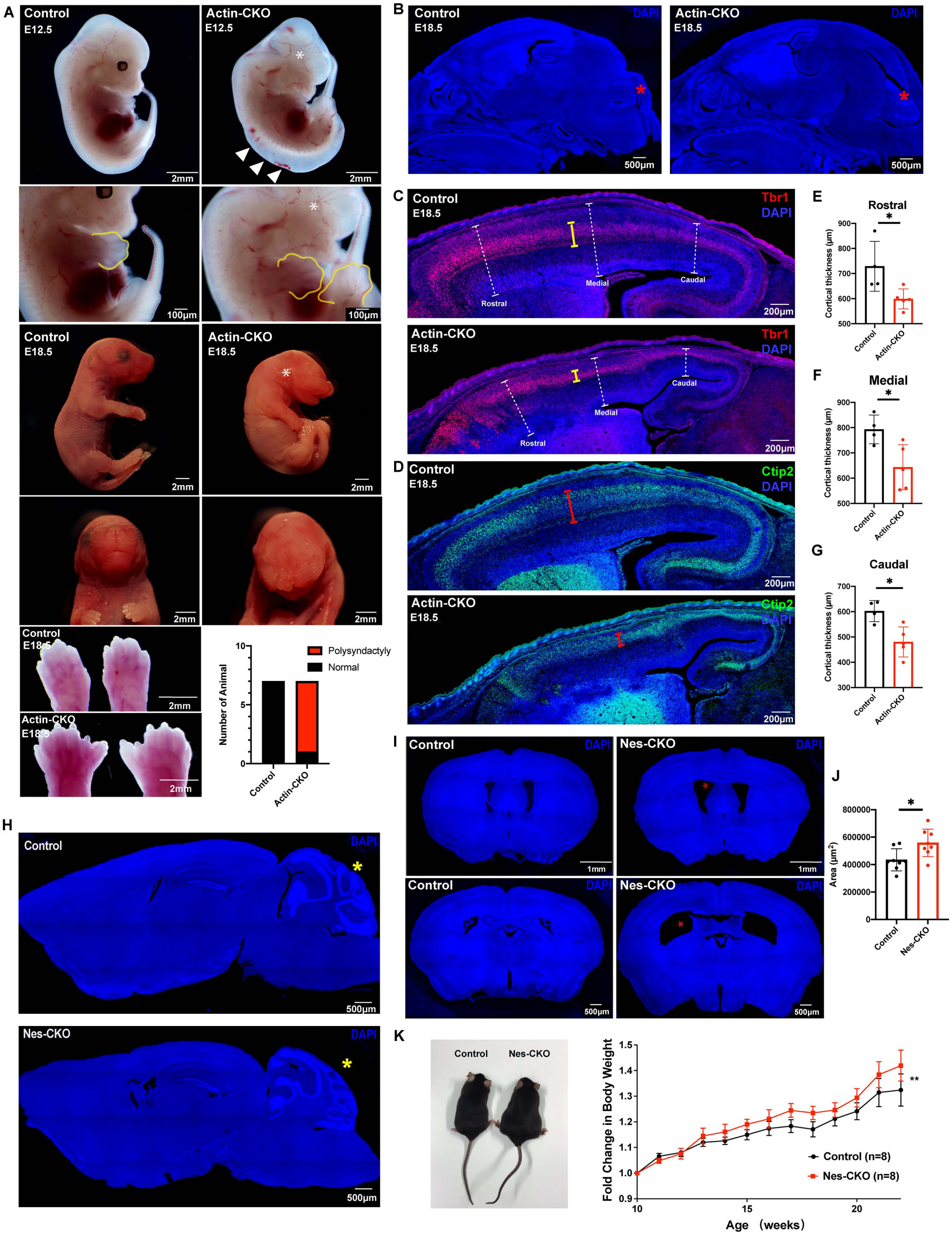

Fig 1. *Rab23*-KO mutants recapitulate the cardinal features of the CS and ciliopathy. (A) Representative images show gross morphological appearance of control and actin-CKO mutant mice at E12.5 (top) and E18.5 (bottom), respectively. White asterisks label missing or deformed eyes in actin-CKO mice, white arrowheads show the mis-patterned posterior neural tube. Bottom panel: representative close-up images of the limbs reveal polysyndactyly in actin-CKO mice at E18.5, a similar abnormality is also observed at E12.5 (yellow outline, second panel from top). Adjacent graph shows

the proportion of mice exhibiting polysyndactyly. (n = 7 per group). **(B)** Representative DAPI-stained images depict mid-sagittal sections of the head regions of E18.5 control and actin-CKO mouse embryos. Mis-patterning of the cerebellar anlage (red asterisk) is observed in the actin-CKO embryo. **(C-G)** Representative mid-sagittal brain sections depict mis-patterned and thinned cerebral cortex (white dashed capped arrow) in the actin-CKO mice, which was associated with a thinning of **(C)** Tbr1+ (yellow capped arrow) and **(D)** Ctip2+ (red capped arrow) post-mitotic neuron layers. Graphs depict the quantification of the cortical thickness in control and actin-CKO mice across **(E)** rostral, **(F)** medial, and **(G)** caudal regions; n = 4–5 per group. Each data point represents the average thickness from 2-3 brain sections per animal. * *P*-value ≤ 0.05, Unpaired Student's t-test. **(H)** Representative DAPI-stained images depict mid-sagittal brain sections of adult control (top) and Nes-CKO (bottom) mice respectively. Cerebellum mis-patterning (yellow asterisk) was observed in adult Nes-CKO mice. **(I-J)** Representative DAPI-stained images depict coronal brain sections of adult control and Nes-CKO mice, revealing an enlargement of brain ventricles (red asterisks) in Nes-CKO mice. The top panel depicts lateral ventricles at the rostral cortex. Bottom panel depicts lateral ventricles at the rostral hippocampus level. **(J)** Quantification of brain ventricular area in adult control and Nes-CKO mice. Each data point represents the average ventricular lumen area measured at the rostral hippocampus level across three brain sections per animal. n = 8 mice per group. * *P*-value ≤ 0.05, Unpaired Student's t-test. **(K)** Representative image and graph show gross morphological appearance and weekly body weight measurements of adult male control and male Nes-CKO mice, respectively. Adult Nes-CKO mice appear obese. Two way ANOVA, ***P* value ≤ 0.01.

https://doi.org/10.1371/journal.pgen.1011611.g001

(GCP), and mature neurons, we conducted immunohistochemistry staining using specific antibodies against Arl13b and Adenylyl Cyclase 3 (AC3). Consistent with our hypothesis, the mutant mice exhibited a notable decrease in the number of cells bearing primary cilium in the cerebral cortex. This trend was consistently observed in both knockout mutants, i.e., including the Tbr1-expressing cortical intermediate progenitors at embryonic stage (E18.5 of actin-CKO), as well as in NeuN-positive cortical neurons in the adult neocortex of the Nes-CKO mutant (Figs 2A, 2B, S4A, S4B, 2M and 2N). Co-immunostaining of adult sagittal brain sections with two ciliary markers, i.e., Arl13b and AC3, along with the neuronal marker NeuN, revealed that the majority of cortical neurons in the Nes-CKO mutant neocortex had lost their primary cilia, whereas cortical neurons in the control animals exhibited a higher level of ciliation (Fig 2M and 2N). In chondrocytes, although there was no discernible change in the prevalence of ciliation, the primary cilia length was significantly reduced (by 16.75%) in the E18.5 actin-CKO mutant, compared to controls (Fig 2G–2I).

Interestingly, unlike that observed in the cortical layer, the neuronal population in the adult hippocampus CA1 region showed a similar number of AC3-positive primary cilia in both the control and the Nes-CKO mutant group (Fig 2M–2P). Similarly, in the E18.5 actin-CKO mutant, a relatively normal prevalence of ciliation was observed in the Pax6-expressing granule cell precursors (GCPs) in the *Rab23*-deficient cerebellar anlage, as well as in E-cadherin expressing epithelial cells lining the dermal layer (Fig 2C–2F). Intrigued by the variable ciliary abnormalities, we examine primary cilia morphology in mouse embryonic fibroblasts (MEFs) culture by co-immunolabelling of Arl13b and Acetylated-α-tubulin (Figs 2J and S4C). The actin-CKO MEFs exhibited unchanged cilia length but a significantly reduced ciliation frequency (Figs 2J–2L and S4C).

In conclusion, these findings provide the first *in vivo* evidence demonstrating that the knockout of *Rab23* selectively disrupts primary cilia formation and/or maintenance in specific neuronal populations and MEFs, while causing a subtle yet significant ciliary morphological defect in chondrocytes. This highlights the critical role of Rab23 in primary cilium-dependent functions in the central nervous system (CNS), fibroblasts, and bone development in mammals. Interestingly, it is noteworthy that not all neuronal cell types show an evident primary cilia defect upon *Rab23* loss, suggesting that the ciliary function of *Rab23* may be context-dependent and influenced by specific neuronal functions.

Morpholino knockdown of *rab23* in zebrafish results in selective deciliation of a restricted brain region

To investigate whether RAB23 may exert conserved ciliary functions across vertebrates, we performed multiple amino acid sequence alignments to examine RAB23 sequence similarity among different species (S1 Fig). The analysis revealed high sequence conservation between human, mouse (Mus musculus), and zebrafish (Danio rerio), with 93.25% identity between human and mouse, and 84.39% between human and zebrafish (S1 Fig). These results demonstrate that RAB23 is highly conserved among these vertebrates, suggesting potentially conserved ciliary functions across these model organisms. Given that the mouse *Rab23* shares 83.12% sequence identity with zebrafish *rab23* (S1 Fig), we investigated further to find out if the functional effects of *Rab23* on the primary cilium are conserved

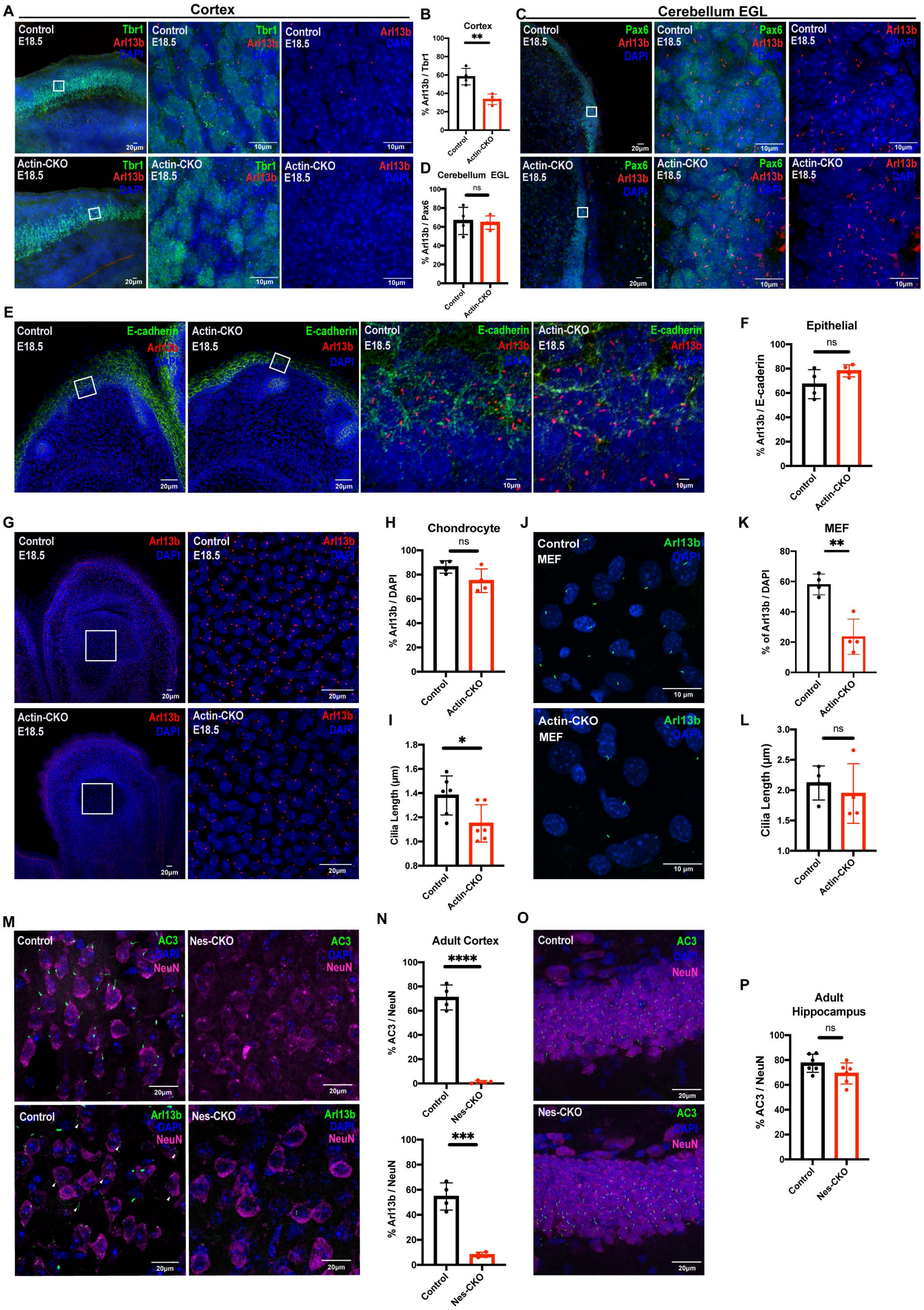

Fig 2. ***Rab23*** **deletion perturbs ciliation in a context-dependent manner. (A-B)** Representative immunohistochemistry images (low power on left, magnification of boxed region on right) and **(B)** graph depicting quantification of the proportion of Arl13b+ primary cilia against Tbr1+ (green) neocortical layer VI neurons in the neocortex at E18.5. A significant two-fold reduction in the number of primary cilia is observed in the cerebral cortex of actin-CKO mouse embryos. Each data point represents the average percentage count across three brain sections per animal. n = 4 per group. ** P-value ≤ 0.01,

Unpaired Student's t-test. **(C-D)** Representative immunohistochemistry images and **(D)** graph depicting quantification of the proportion of Arl13b+ primary cilia against Pax6+ (green) granule cell precursors in the external granule layer (EGL) of cerebellum anlage at E18.5. Each data point represents the average percentage across 2-3 brain sections per animal. n = 4 per group. n.s. = not significant. Unpaired Student's t-test. **(E-F)** Representative immunohistochemistry images and **(F)** graph depicting quantification of the proportion of Arl13b+ primary cilia against E-cadherin+ (green) epithelial cells lining the epidermal layer at E18.5. Each data point represents the average percentage across 2-3 brain sections per animal. n = 4 per group. n.s. = not significant. Unpaired Student's t-test. **(G-H)** Representative immunohistochemistry images of E18.5 digits and **(H)** graph depicting quantification of the proportion of Arl13b+ primary cilia against chondrocytes residing in the phalanges. Each data point represents the average percentage across 3-4 brain sections per animal. n = 4 per group. n.s. = not significant. Unpaired Student's t-test. **(I)** Graph depicting the measurements of cilia length in the chondrocytes of control and actin-CKO at E18.5. Graph illustrate data from 6 biological replicates in each genotype. Each data point represents the average cilia length of 150–200 cilia measured in each animal. For each animal sample, the data was collected from 3-4 images of comparable regions of interest. $^{*}P$ value ≤ 0.05. Unpaired Student's t-test. **(J-K)** Representative immunocytochemistry images and **(K)** graph depicting quantification of the proportion of Arl13b+ (bottom panel green) primary cilia in the mouse embryonic fibroblasts cultured from E12.5 control and actin-CKO respectively. Each data point represents the percentage of ciliation of each independent experiment. Data represents four independent experiments. $^{**}P$ value ≤ 0.01. Unpaired Student's t-test. **(L)** Graph depicts the measurements of cilia length in the mouse embryonic fibroblasts cultured from control and actin-CKO respectively. Data represents four independent experiments. Each data point represents the average cilia length of 20-30 cilia measured in each genotype from each independent experiment. n.s. = not significant. Unpaired Student's t-test. **(M-N)** Representative immunohistochemistry images and **(N)** graphs depicting quantification of the proportion of AC3+ (top panel green) or Arl13b+ (bottom panel green) primary cilia against NeuN+ (pseudo-colored magenta) neurons in cerebral cortex of control and Nes-CKO mice aged 2-3 months. White arrowheads indicate primary cilia weakly express Arl13b. Similar to actin-CKO mice, neural progenitor cell-specific *Rab23* knockout mutants show dramatically decreased number of ciliated neurons in the cerebral cortex of the animals. Each dot represents the average percentage across 2-3 brain sections per animal. n = 4 per group. **** P value ≤ 0.0001. Unpaired Student's t-test. **(O-P)** Representative immunohistochemistry images and **(P)** graph depicting quantification of the proportion of AC3 + primary cilia against NeuN+ neurons in the hippocampal CA1 cells of both control and Nes-CKO mice. n = 4-5 mice in each genotype. For each sample, the percentage of ciliated cells was determined from 3-5 images of comparable regions of interest. n.s. = not significant. Unpaired Student's t-test.

https://doi.org/10.1371/journal.pgen.1011611.g002

in the zebrafish model. To knock down the *rab23* homolog in zebrafish, we designed a morpholino (MO) oligonucleotide targeting the splicing site at the exon 2-intron 2 border of *rab23* to block proper splicing of *rab23* mRNA. This splicing-blocking MO was expected to cause either complete or partial deletion of exon 2, leading to the production of defective mRNA transcripts. The efficiency and specificity of the splicing blocker MO were assessed using reverse transcription polymerase chain reaction (RT-PCR). Indeed, at 24 hpf following injection of MO, we observed that while the level of internal loading control (i.e., *actin*) remains relatively unchanged (Fig 3B, lower panel, 206 bp), the amount of spliced *rab23* product was greatly reduced, with very little aberrant spliced product detectable (Fig 3B, upper panel). This result suggests that the MO effectively blocked the proper splicing of *rab23*, resulting in a depletion and/or generation of defective *rab23* transcript.

A slight but significant head size difference was observed between the controls and *rab23* morphants, in which the head size of *rab23* morphants was larger than that of controls (Figs 3A and S3). In zebrafish, motile cilia are predominantly localized to the pronephric duct and Kupffer's vesicle. In contrast, both motile and primary cilia are present in the brain ventricles, specifically, motile cilia on ependymal cells (for cerebrospinal fluid flow) and primary cilia on neuroepithelial/neural progenitor cells. These ciliated cell types line the neural tube ventricular system, spanning the anterior neural tube at the forebrain to the posterior neural tube at the spinal cord.

We examined the motile and primary cilia by performing whole-mount immunostaining of acetylated-α-tubulin at 24 hpf. Our results showed that there was no discernible change in motile cilia number in the pronephric duct (Fig 3D), and no significant reduction in the number of cilia lining the central canal of the spinal cord (Fig 3C). Interestingly, a prominent reduction in the number of cilia was observed in the forebrain ventricle of *rab23* morphants. Quantification along the ventricle lining region (Fig 3E, dotted line boxes) revealed that the percentage of ciliated cells in the forebrain ventricle of *rab23* morphants reduced to approximately 40%, whereas there were about 70% ciliated cells in the control counterpart (Fig 3E). To rule out potential off-target effects of the morpholino, we performed a rescue experiment by co-injecting MO with *rab23* mRNA and quantified the cilia number (Fig 3E). There was a significant recovery in the number of primary cilia in the rescue group as compared to the morphant without *rab23* mRNA (Fig 3E), confirming that the decrease in the percentage of ciliation was due to the loss of *rab23.*

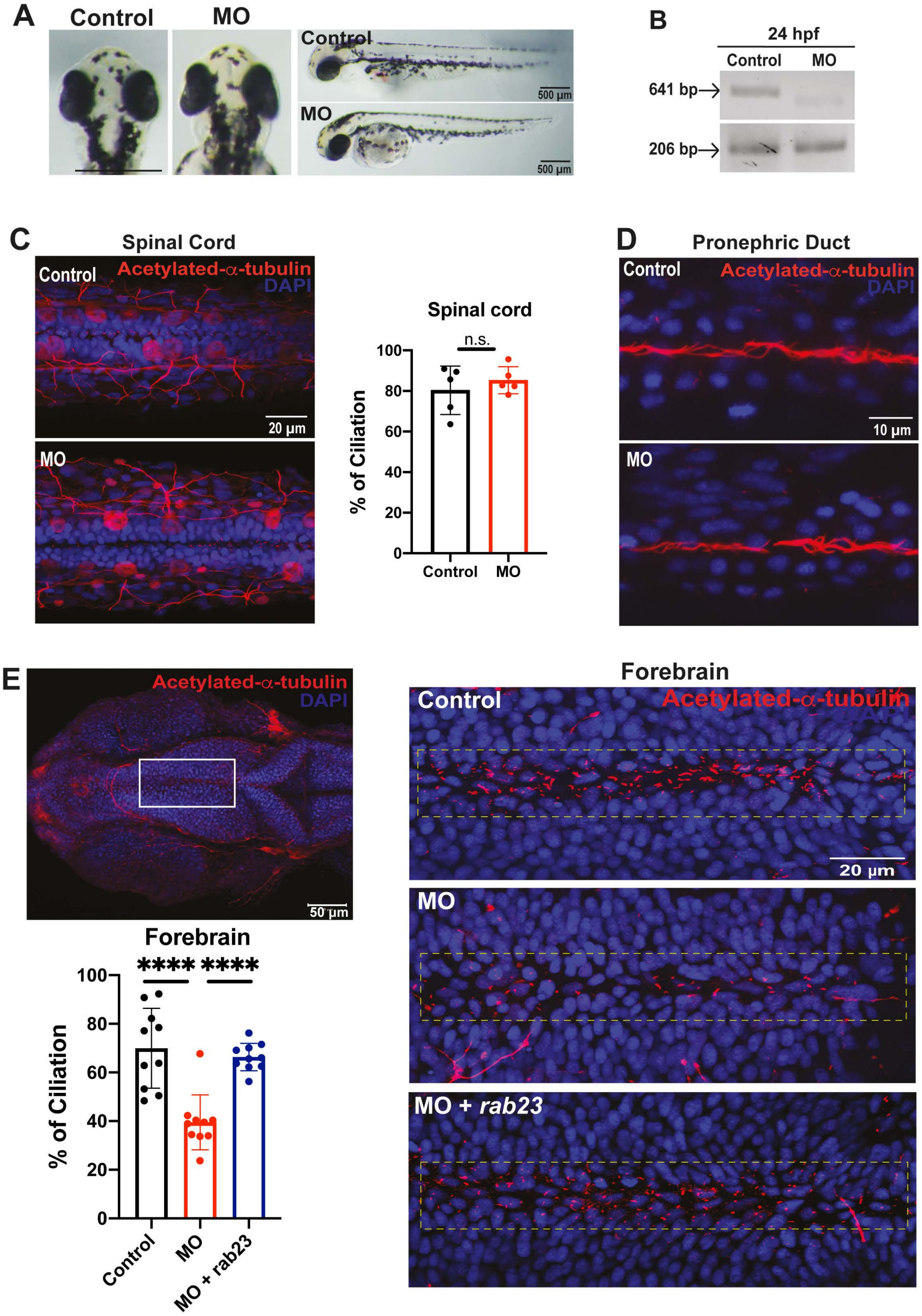

Fig 3. Knockdown of *rab23* in zebrafish affects primary cilia formation at the rostral brain ventricle. (A) Morpholino-mediated knockdown of *rab23* in zebrafish. Bright-field dorsal view microscopy images of control and morphant (MO) at 72 hpf. **(B)** Representative gel image showing normal splicing of *rab23* in control (641 bp) or inhibited splicing in morphants 24 hour-post-fertilization (hpf), resulting in less or shorter spliced product. Actin (206 bp) was used as the internal control. **(C)** Representative images and graph showing largely unaffected percentage of cilia lining the central canal

of the spinal cord between control and morphant. n = 5 animals for each group. Error bars depict S.D. n.s. = not significant. Unpaired Student's t-test. **(D)** Representative images showing largely unaffected cilia number at the central canal of the pronephric duct between control and morphant. **(E)** Representative images showing an obvious reduction of cilia number present in the forebrain ventricle of morphant as compared to control. Bottom right: rab23 morphant rescued by injecting mRNA of *rab23* (bottom panel). Bottom left panel: Graph presenting quantitative analysis of cilia number in the brain ventricle of control, morphants and rescue group at 24 hpf, respectively. n = 10 for each group. Error bars depict S.D. **** P value ≤ 0.0001 One-way ANOVA.

https://doi.org/10.1371/journal.pgen.1011611.g003

Thus, in line with the observations in our mouse mutants, silencing *rab23* in zebrafish also resulted in a perturbation of primary cilia in specific cell types and neuronal lineages/populations. In particular, our data revealed that zebrafish *rab23* exerts paramount ciliary functional effects in the ependymal cells and neural progenitor cells residing in the forebrain but not in the spinal cord.

Neural progenitor cells and neurons differentiated from Carpenter syndrome patient iPSCs exhibit impaired formation of the primary cilium

We then investigated whether *RAB23* also plays a role in regulating the primary cilia formation in neuronal cells of human origin. For this purpose, we obtained patient-derived skin fibroblast cells carrying a biallelic p.(L145*) variant with a nonsense mutation in the *RAB23* gene [8,9]. These fibroblast cells were reprogrammed into induced pluripotent stem cells (iPSC) clones. The successfully reprogrammed iPSC clones exhibited a normal karyotype profile, and their pluripotency was confirmed by abundant expression of human stem cell markers SSEA4, NANOG, OCT3/4, and TRA-1–60 (Fig 4A–4C, images represent results of patients-iPSCs with p.(L145*) variant).

We examined the primary cilia in patient iPSCs, iPSC-induced neural progenitor cells (hNPC), iPSC-differentiated neurons, and patient fibroblasts. Normal fibroblasts and iPSCs reprogrammed from healthy human dermal fibroblasts were used as the respective controls. Interestingly, the patients' iPSCs, fibroblasts, and neural progenitor cells exhibited a significant reduction in the length of the primary cilium axoneme, despite an unaffected percentage of ciliation (Figs 4D–4I, 4L, 4M and S5). On the other hand, the neurons from p.(L145*) variant exhibited a significantly reduced ciliation prevalence (reduced by 89.83%, Fig 4J and 4K). These findings indicate that *RAB23* plays an important roles in promoting ciliogenesis in neurons, and maintaining proper cilia length in human iPSCs, hNPC and fibroblasts. Collectively, these results further suggest that the loss of *RAB23* function causes a ciliopathy in humans.

Rab23 plays critical roles in neuronal primary cilium formation and elongation

Given the profoundly reduced cilia prevalence in *Rab23*-KO neurons, we sought to further elucidate Rab23's role in neuronal primary cilia. Using primary cortical neurons cultured from P0 cortices, we examined progressive changes in cilia prevalence and elongation during neuronal maturation (Fig 5). While control neurons displayed time-dependent and progressive increases in both cilia prevalence and length, *Rab23*-KO neurons from Nes-CKO mutants exhibited persistently reduced ciliation and shorter cilia throughout the 18-day culture period as compared to the control group (Fig 5A–5C). Intriguingly, KO neurons showed relatively mild ciliary disruptions at DIV 3, with increasingly severe perturbations emerging as neurons developed more elaborate projections. These findings strongly suggest Rab23's critical roles in primary cilium formation and elongation in neurons.

Loss of *Rab23* impairs primary cilium-dependent Sonic Hedgehog signaling pathway activation in the neural progenitor cells

We hypothesize that the decrease in ciliation disrupts the signal transduction of primary cilium-dependent Shh signaling pathway, potentially playing a role in the phenotypical abnormalities and developmental defects observed in the *Rab23*-KO mutant and Carpenter syndrome patients. To investigate this, we examine the ciliation prevalence, and

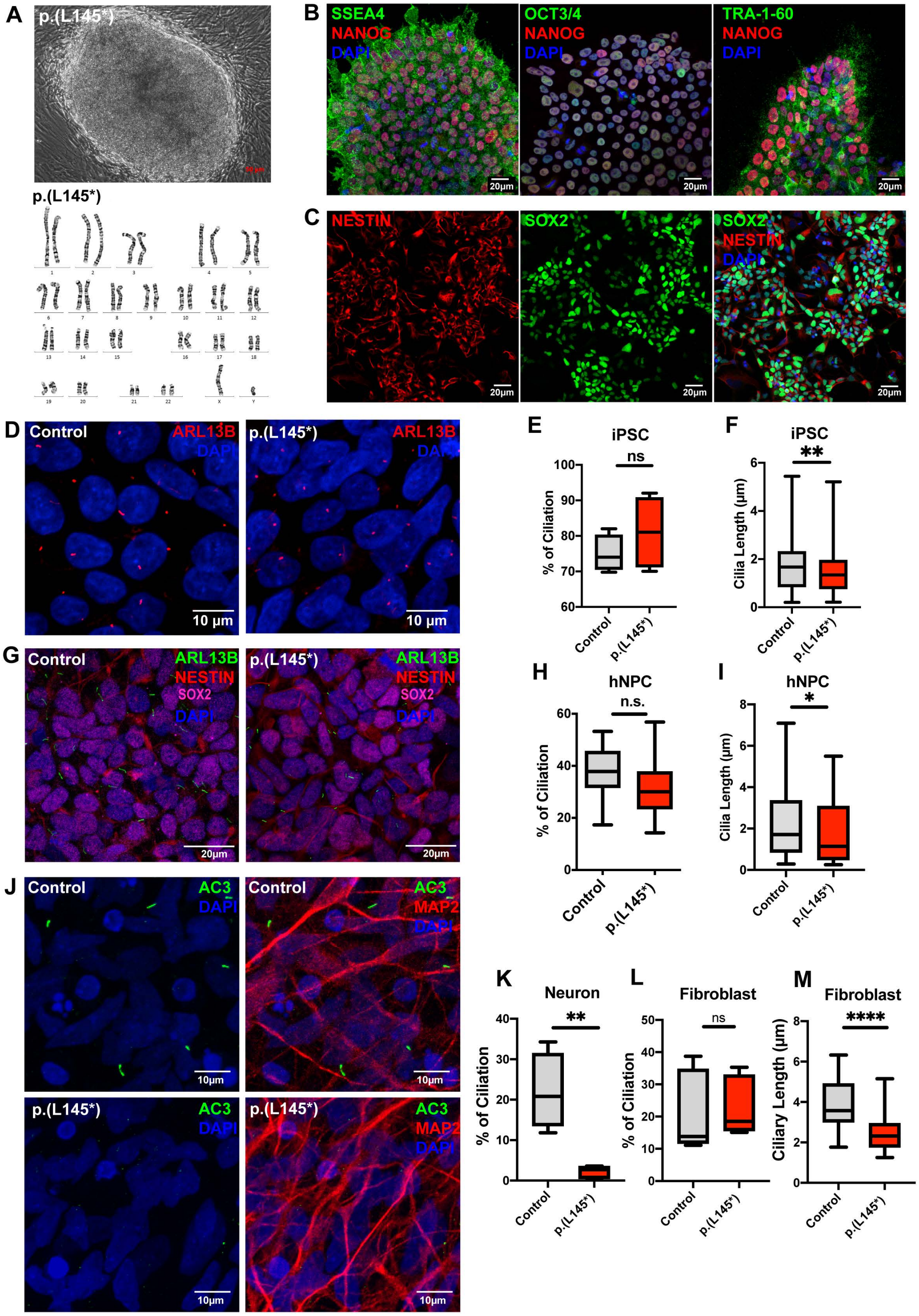

Fig 4. Carpenter syndrome patient-derived iPSC-differentiated neurons exhibit severely impaired ciliogenesis. (A-B) Fibroblasts isolated from skin biopsy from a Carpenter syndrome patient bearing the *RAB23* biallelic p.(L145*) variant was reprogrammed into iPSC clones. **(A)** Top: A representative phase contrast image showing successfully reprogrammed-iPSC clone displaying a normal karyotype (bottom), and pluripotency characterized by

positive **(B)** co-immunostainings of human stem cell markers SSEA4, NANOG, OCT3/4 and TRA-1-60 respectively. **(C)** Representative co-immunocytochemistry images depicting positive expression of NESTIN (red) and SOX2 (green) on neural progenitor stem cells induced from iPSCs. **(D)** Representative co-immunocytochemistry images depicting the iPSCs of healthy adults (control) and Carpenter syndrome patients (p.(L145*)). Cells were immunostained for the primary cilia marker ARL13B (red). **(E)** Graph depicts the quantification of the percentage of ciliation in iPSCs. Box plot represents data from four independent experiments. n.s. = not significant. Unpaired Student's t-test. **(F)** Box plots depict the measurements of cilia length on iPSCs. Data represents the measurements of ~80-90 cilia in each genotype obtained from four independent experiments. ** P value ≤ 0.01. Unpaired Student's t-test. **(G)** Representative co-immunocytochemistry images depicting healthy adult and Carpenter syndrome patient iPSC-derived human neural progenitor cells (hNPCs) co-immunostained for SOX2 (magenta), NESTIN (red) and primary cilia marker ARL13B (green). **(H)** Graph depicts the quantification of the percentage of ciliation in hNPCs. Box plot represents data from at least five independent experiments. n.s. = not significant. Unpaired Student's t-test. **(I)** Box plot depicts the measurements of cilia length on hNPCs. Data represents the measurements of ~65–80 cilia in each genotype obtained from at least three independent experiments. *P value ≤ 0.05. Unpaired Student's t-test. **(J-K)** Representative co-immunocytochemistry images depict MAP2+ (red) neurons differentiated from iPSCs of healthy adults (control) and Carpenter syndrome patients (p.(L145*)). Primary cilia were labelled by AC3 (green). **(K)** Graph depicts the percentage of ciliation, i.e., quantification of the proportion of ciliated neurons (AC3 + MAP2+) in the MAP2 positive neuronal population. A significant reduction in ciliation was observed in neurons bearing p.(L145*) variant. Box plot represents data from four independent experiments. ** P value ≤ 0.01 Unpaired Student's t-test. **(L)** Graph depicts the quantification of the percentage of ciliation in primary fibroblast cells. The primary cilia in human fibroblast were visualised by immunostaining of acetylated-alpha-tubulin and ARL13B. Primary fibroblasts cultured from a healthy donor and a Carpenter syndrome patient with p.(L145*) variant show comparable percentages of ciliation. Box plot represents data from five independent experiments. n.s. = not significant. Unpaired Student's t-test. **(M)** Box plot depicts the measurements of cilia length on fibroblast. Data represents the measurements of ~65–80 cilia in each group obtained from five independent experiments. ****P value ≤ 0.0001. Unpaired Student's t-test.

https://doi.org/10.1371/journal.pgen.1011611.g004

measure the response of *Rab23*-KO cortical neural progenitor cells (NPCs) to the stimulation of the Shh signaling pathway in primary culture. Consistent with the *in vivo* findings in the cerebral cortex of the E18.5 actin-CKO mutant (Fig 2A), an apparent reduction in the percentage of ciliated cells was observed in the *Rab23*-KO primary cortical NPCs culture isolated from Nes-CKO mutant (Fig 6A and 6B). Additionally, akin to the observations in the human NPCs derived from the Carpenter syndrome patient iPSCs, the cortical NPCs cultured from *Rab23*-KO mice also exhibit a shortened cilia length (Fig 6B).

After confirming the structurally defective primary cilia in *Rab23*-deleted NPCs culture, we employed SAG, a Smoothened (Smo) agonist, to evaluate the sensitivity of the NPCs to the primary cilium-dependent activation of Shh signaling pathway. SAG triggers the Shh signalling pathway by promoting the Smo translocation to the primary cilium axoneme, thereby activating the primary cilium-dependent Shh signaling pathway. Therefore, a dysfunctional primary cilium would render the cell becoming unresponsive to SAG stimulation. A green fluorescence protein (GFP) Gli reporter system was used to determine the level of Shh signalling pathway activation based on the level of Gli activity.

In line with our speculation, *Rab23*-KO neural progenitor cells did not exhibit responsiveness to the SAG stimulation, showing no discernible change in the Gli reporter activity level following a 24 hour stimulation with 200 nM SAG. Conversely, the control (*f/f*) mouse neural progenitor cells demonstrated a significantly increased level of Gli reporter activity as compared to the DMSO vehicle control group, indicating a robust response and activation of the Shh signaling pathway (Fig 6E). These findings suggest that the loss of *Rab23* impairs the NPCs' response to primary cilium-dependent Shh signaling pathway activation due to dysfunctional primary cilia.

Notably, in the absence of SAG stimulation, *Rab23*-KO NPCs at basal level (DMSO) showed an up-regulated Gli activity compared to the control group (Fig 6E, Control+DMSO versus Nes-CKO+DMSO). This observation is consistent with our previous observations in cerebellar granule progenitor cells [18,35], and aligned with the well-established negative regulatory role of *Rab23* in the Shh signalling pathway [16]. Consistent with the Gli reporter assay results, qPCR analysis of gene expression also revealed ectopic activation of the Shh signaling pathway in the mutant NPCs, as evidenced by elevated *Gli1* expression (a downstream transcriptional readout of Shh signaling activity) (Fig 6F). Interestingly, despite the elevated *Gli1* expression, the expression levels of *Shh,* NPC markers, i.e., *Nestin* and *Sox2,* and the cell proliferation marker *Ki67,* remained unchanged (Fig 6F). These results may suggest a partial activation of the Shh signaling pathway following the deletion of *Rab23* in NPCs.

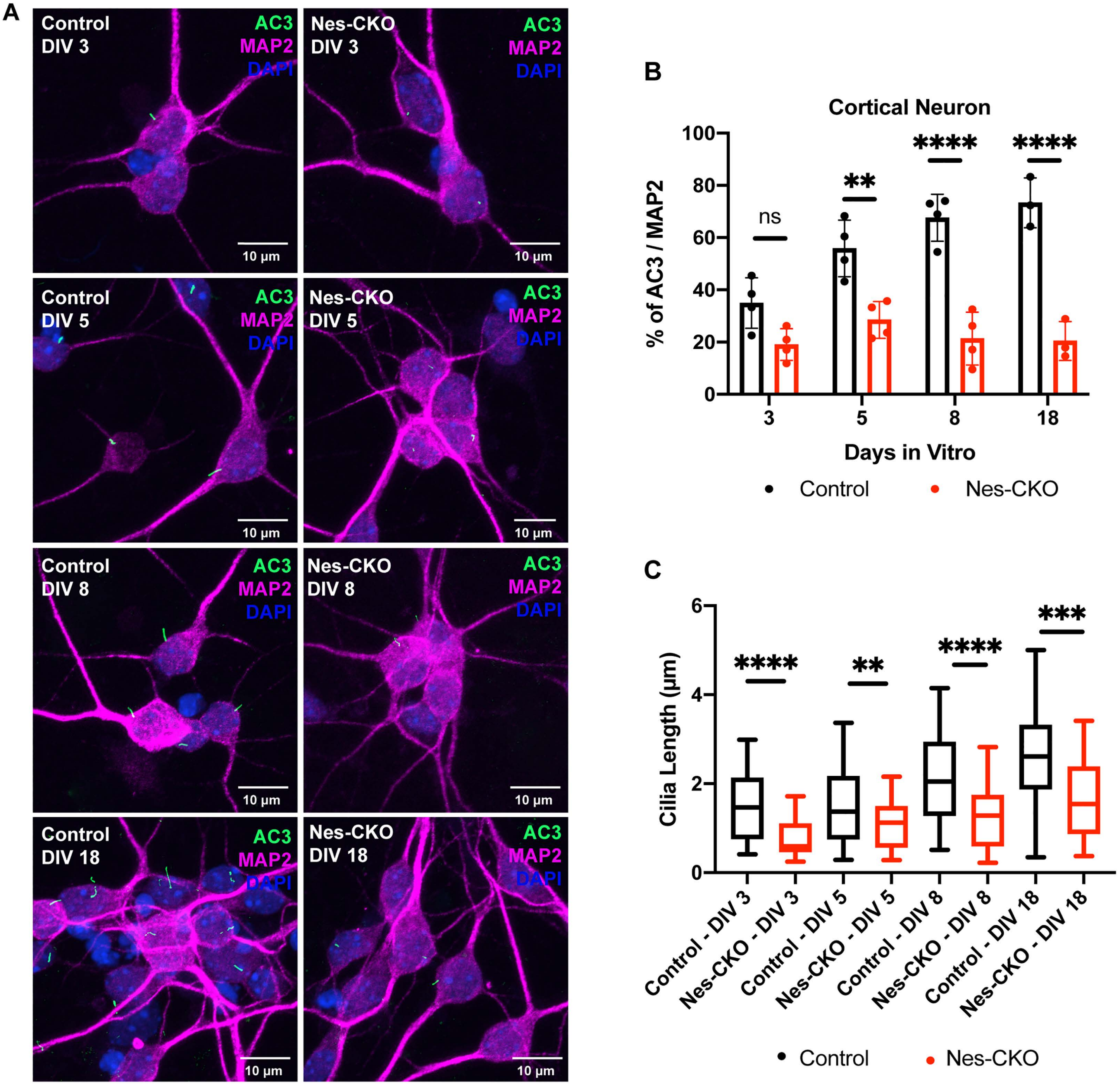

Fig 5. ***Rab23*** **plays critical roles in neuronal primary cilia formation and elongation. (A)** Representative co-immunocytochemistry images depict the process of primary cilia elongation in the control and Nes-CKO primary cortical neuron cultures at DIV 3 to DIV18. Neurons were co-immunostained for MAP2 (magenta), and the primary cilia marker AC3 (green) respectively. **(B)** Graph depicts the percentage of ciliation, i.e., quantification of the proportion of ciliated neurons (AC3 + MAP2+) in the MAP2 positive neurons. Data represents three to four independent experiments. n.s. = not significant, ** *P* value $\leq$ 0.01, **** *P*-value ≤ 0.0001, two-way ANOVA. **(C)** Graph depicts the measurement of cilia length of primary cortical neurons cultures at DIV 3 to DIV18. Box plot represents data of ~70–80 cilia in each group obtained from three to four independent experiments. ** *P* value $\leq$ 0.01, *** *P* value $\leq$ 0.001, **** *P*-value ≤ 0.0001, two-way ANOVA.

https://doi.org/10.1371/journal.pgen.1011611.g005

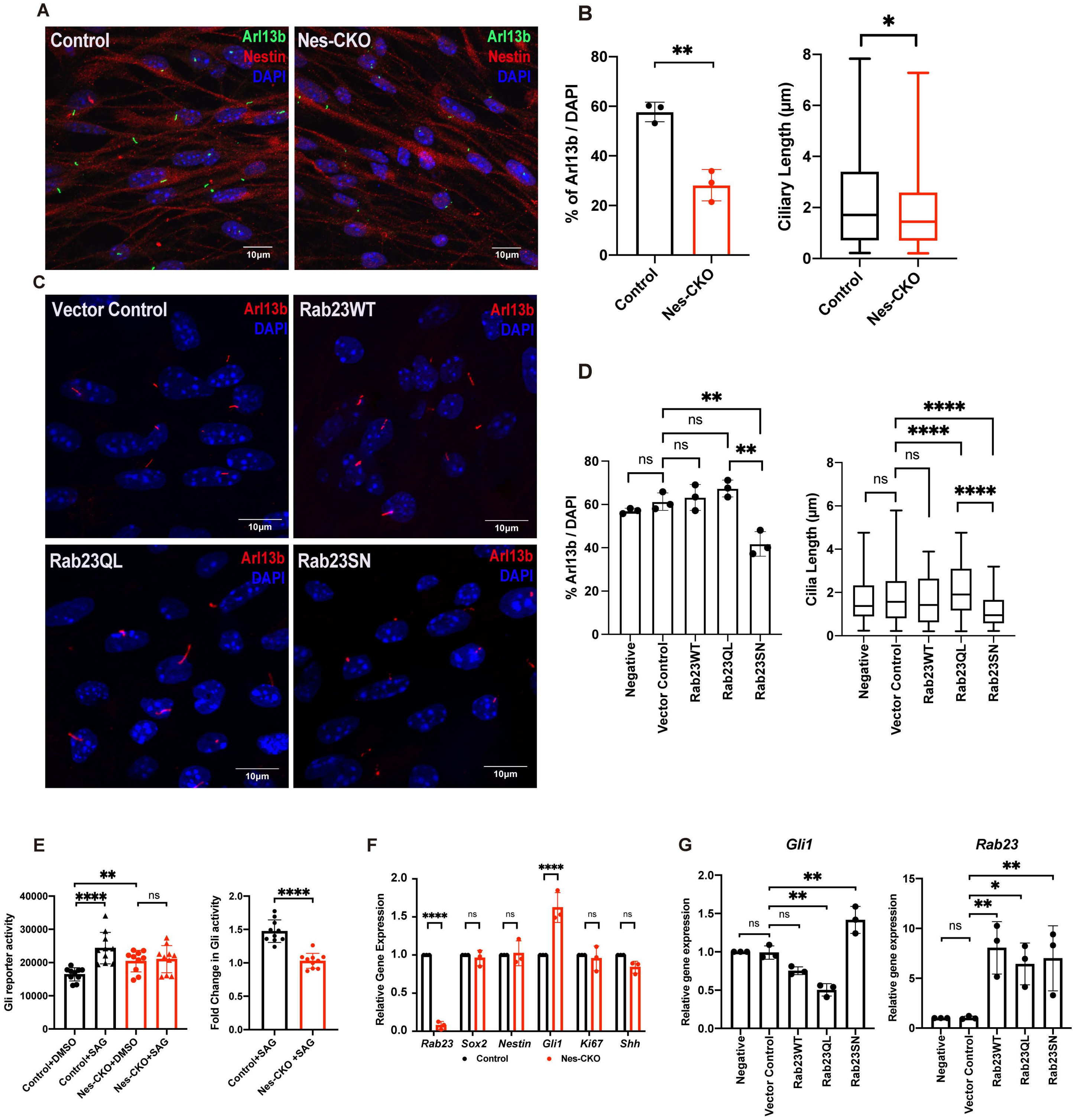

Fig 6. ***Rab23*-deleted murine neural progenitor cells show disrupted ciliation and compromised response to Smo-dependent Hedgehog signaling pathway activation. (A)** Representative immunocytochemistry images depict control and Nes-CKO cortical NPCs immunostained for Nestin (red) and primary cilia marker Arl13b (green). **(B)** Graphs depict the quantification of the percentage of ciliation and cilia length in mouse cortical neural progenitor cells culture. For the ciliation, each dot represents the average percentage value of each independent experiment. For length measurement,

data represents the measurements of ~200-230 cilia in each genotype obtained from four independent experiments.** *P*-value ≤ 0.01. Unpaired Student's t-test. **(C)** Representative co-immunocytochemistry images depicting wild-type cortical NPCs overexpressing wild-type and mutant forms of Rab23 at day 3 post-transduction. NPCs were immunostained for primary cilia marker Arl13b. **(D)** Graph depicts the quantification of the percentage of ciliation in wild-type cortical NPCs at day 3 following overexpression of either wild-type full-length Rab23 or its mutant forms. Box plot represents data from 3 independent experiments. Box plot depicts the measurements of cilia length on NPCs. Data represents the measurements of ~70–80 cilia in each group obtained from three independent experiments. ** *P*-value ≤ 0.01, **P*-value ≤ 0.05, two-way ANOVA. **(E)** Graphs depict the (left) 7Gli:GFP reporter signals and the (right) relative fold-change in control and Nes-CKO cortical NPCs treated with 200 nM SAG and DMSO respectively for 24 hours. Data points represent triplicate readings from three independent experiments. Left: **** *P*-value ≤ 0.0001, ** *P*-value ≤ 0.01, n.s. = not significant, two-way ANOVA. Right: **** *P*-value ≤ 0.0001, Unpaired Student's t-test. **(F)** Graph depicts the relative gene expression level of control and Nes-CKO cortical NPCs quantified by real-time qPCR. **** *P*-value≤0.0001, n.s. = not significant, two-way ANOVA. **(G)** Graphs depict the relative gene expression levels of *Gli1* and *Rab23* in wild-type cortical NPCs overexpressing wild-type and mutant forms of Rab23 at day 6 post-transduction. NPCs were transduced with lentiviruses carrying different overexpression construct, i.e., Rab23WT, Rab23Q68L, Rab23SN respectively. The gene expression levels of *Gli1* and *Rab23* at day 6 post-transduction were quantified by real-time qPCR. ** *P*-value ≤ 0.01, n.s. = not significant, one-way ANOVA.

https://doi.org/10.1371/journal.pgen.1011611.g006

While Rab23 is known for its role in modulating the Shh signaling pathway, it has remained unclear whether this function requires its GTP/GDP cycling-dependent property, which is a classical molecular characteristic of small GTPases. To address this, we overexpressed wild-type full-length Rab23, constitutively active (GTP-bound) form of Rab23, i.e., Rab23Q68L, and dominant negative (GDP-bound) form of Rab23, i.e., Rab23S23N in wild-type NPCs, respectively. The *Gli1* expression levels were then measured and compared between these overexpression groups. The data showed that the overexpression of Rab23Q68L in wild-type mouse cortical NPCs led to a decrease in the expression of *Gli1*. Conversely, overexpressing the dominant negative (GDP-bound) form of Rab23, specifically Rab23S23N, resulted in an increase in *Gli1* expression (Fig 6G), similar to the observations in *Rab23*-Nes-CKO NPCs (Fig 6F). These results indicate that Rab23 modulates Shh signaling activity through its classical GTP/GDP cycling-dependent functions, presumably involving its specific guanine nucleotide exchange factor (GEF) and GTPase-activating protein (GAP).

We further analyzed both ciliation percentage and cilia length (Fig 6C and 6D) while investigating Rab23 overexpression effects on Hedgehog signaling. Overexpression of Rab23WT in wild-type NPCs showed no significant changes in ciliation prevalence or cilia length compared to controls. Whereas, the constitutively active Rab23QL form maintained normal ciliation prevalence but displayed significantly longer cilia relative to both controls and the Rab23SN inactive group. Conversely, overexpression of the constitutively inactive Rab23SN mutant resulted in significantly shorter cilia and reduced ciliation frequency compared to both vector controls and Rab23QL-expressing NPCs (Fig 6C and 6D). Interestingly, these findings reveal opposing trends between cilia morphology and Hedgehog signaling activity following Rab23 overexpression, with constitutively active Rab23QL increasing cilia length while decreasing Hh signaling, and inactive Rab23SN producing shorter cilia with elevated Hh pathway activity.

Discussion

Our study underscores the critical and evolutionarily conserved functions of *RAB23* in preserving morphologically intact and functional primary cilia across various vertebrates, including the zebrafish, mice, and humans, notably in a cell type distinctive manner (Fig 7). This study unveils that conditional knockout mouse mutants of *Rab23* exhibit a spectrum of phenotypic and pathological traits reminiscent of the classical clinical features reported in both Carpenter syndrome and ciliopathy disorders in humans. Consistent with the phenotypic association with ciliopathy, examination of primary cilia in both tissue sections and primary culture samples from E18.5 and adult *Rab23* conditional KO mice revealed profound ciliary anomalies in selective mature neuronal populations; and relatively moderate yet statistically significant ciliary perturbations in embryonic fibroblasts, cortical neural progenitor cells, cortical intermediate progenitor neurons, and chondrocytes. In resonance with the structurally perturbed primary cilia, *Rab23*-KO mouse neural progenitor cells also displayed dysfunctional primary cilia, as evidenced by the desensitised response to the primary cilium-dependent activation of the

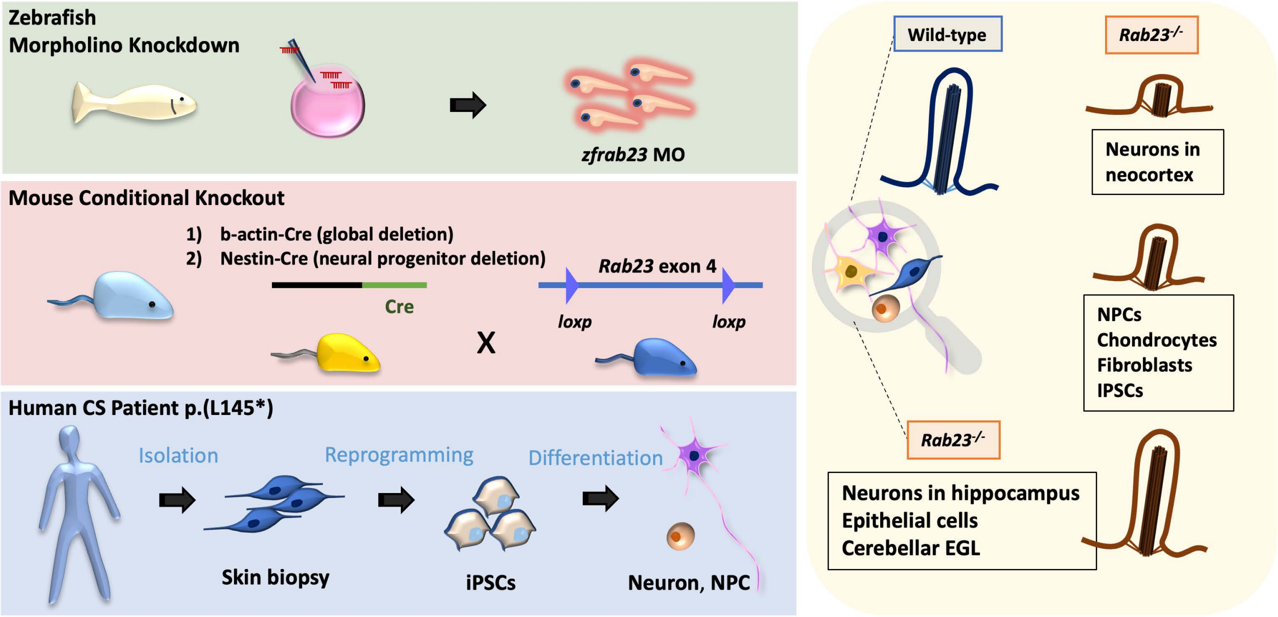

Fig 7. Schematic illustration of the conserved functions of Rab23 in primary cilia. *Rab23* exerts evolutionarily conserved and context-specific functions in maintaining morphologically intact and functional primary cilia. Specifically, in the absence of *Rab23*, severe perturbations in ciliogenesis were found in distinct neuronal populations in the neocortex, while neural progenitor cells, chondrocytes, fibroblasts and iPSCs, were less severely affected. No significant changes in primary cilia prevalence were observed in *Rab23* knockout hippocampus neurons, epithelial cells, or cerebellar granule cell precursors.

https://doi.org/10.1371/journal.pgen.1011611.g007

Hh signaling pathway (Fig 6E). These results further suggest that dysfunctional primary cilia, to some extent, may underlie the pathological presentation of Carpenter syndrome.

Considering the important roles of Rab23 in ciliary trafficking, earlier studies have speculated on the potential connection between Rab23 and ciliopathy [14,19–21,35]. However, as far as our current knowledge extends, there remains a lack of direct evidence substantiating the causal link between *RAB23* mutation and Carpenter syndrome with ciliopathy. Our data reveals for the first time that Carpenter syndrome patients carrying the biallelic *RAB23* p.(L145*) variant exhibit variable degrees of primary cilia anomalies in their tissue samples-derived iPSCs, iPSC-differentiated neurons, neural progenitor cells and fibroblasts. Notably, the most severe ciliary defects was observed in iPSC-differentiated neurons, which showed a drastically reduced ciliation percentage, while patients' iPSCs, hNPCs and fibroblasts exhibited shortened cilia length despite unchanged primary cilia prevalence. Importantly, our collective results show that different vertebrate models of *RAB23* loss-of-function mutants consistently presented with several pathological phenotypes and cellular characteristics typical of human ciliopathies. Our work thus provides compelling and direct evidence demonstrating that *RAB23* mutation is clinically linked to ciliopathy, further validating the classification of Carpenter syndrome as one of the disorders within the ciliopathy spectrum.

Intriguingly, *Rab23* deficiency differentially perturbs primary cilium morphology in a cell type-specific manner, with particularly pronounced effects on certain neuronal populations. This cell-type-specific phenomenon was consistently observed in both *in vivo* mouse and zebrafish models, as well as the Carpenter syndrome patient-derived cells. Importantly, our findings on the context-dependent ciliary function of *Rab23* help to explain the discrepancies previously noted in independent studies where primary cilium defects were reported in some experimental models but not in others [15,19,36]. To examine the structural damage and/or the loss of primary cilia, multiple primary cilium markers were employed for cilia examinations in this study. For example, ciliary membrane markers including ARL13B and AC3, along with the ciliary microtubule marker, Acetylated-α-tubulin, were utilized to visualize the primary cilia axoneme in different cell and tissue samples. Specifically, ARL13B and Acetylated-α-tubulin were used simultaneously to examine primary cilia in multiple cell types, including human iPSCs, MEFs, human dermal fibroblasts, and neocortical intermediate progenitor neurons *in vivo*. Our results demonstrate that Acetylated-α-tubulin co-expresses with ARL13B along the ciliary axoneme in both control and *Rab23* loss-of-function groups across these cell types. While these results confirm the shortening of primary cilia and disrupted ciliogenesis in these cells-types, they do not rule out the possibility that loss of *Rab23* functions could lead to cell-type-specific reduced expression levels of ciliary membrane markers and other ciliary proteins along the axoneme. Notably, in fibroblasts, the results revealed unexpected differences in the ciliary phenotypes between the mouse and human disease models. *Rab23*-KO MEFs exhibited a significantly reduced ciliation percentage without discernible changes in cilia length. In contrast, Carpenter syndrome (CS) patient fibroblasts showed milder ciliary defects, maintaining normal primary cilia prevalence but displaying shortened primary cilia. We reason that these phenotypic inconsistency could be due to differences in the characteristics and tissue origins of the two fibroblast cultures. Specifically, the patient fibroblasts were derived from dermal tissue, whereas the *Rab23*-KO fibroblasts were embryonic fibroblasts originated from embryonic mesoderm.

By scrutinizing the time-dependent changes in cilia prevalence and elongation in primary cortical neuron cultures, our findings strongly suggest pivotal roles of *Rab23* in primary cilium formation and elongation processes in neuron. In agreement with the *in vivo* observations in E18.5 neocortical intermediate progenitor neurons and adult neocortical neurons, primary cortical neurons cultured from *Rab23*-KO mutant displayed relatively milder cilia phenotype disruptions during early culture stages, with more pronounced and severe ciliary perturbations emerging later in more mature neurons. This evidence clearly demonstrates that *Rab23* plays significant roles in primary cilium formation and elongation processes. In addition, our data appears to align with previous study in hTERT-RPE1 cells where Rab23 and its GEF complex were found to act at an intermediate to late stage of cilium formation [15]. Nonetheless, we acknowledge that current evidence remains insufficient to exclude or define potential additional functions of *Rab23* in cilium maintenance or resorption, thus warrants further investigations.

Previous findings reported that the *Rab23*$^{-/-}$ null mutant displayed morphologically normal primary cilia in early embryonic stages, including the Arl13b+ primary cilia in E8.5 mesoderm, and nodal cilia at the 0–1, 3–4, and 5–6 somite stages [36]. Notably, previous studies did not investigate the ciliary functions of *Rab23* at later developmental stages because the *Rab23*$^{-/-}$ null mutant embryos in the C3Heb/FeJ background did not survive beyond E13.5 [16,36]. Here, we employed a Cre-loxp transgenic knockout approach, i.e., using actin-Cre to drive the global deletion; and Nestin-Cre for neural progenitor cells-specific deletion of *Rab23* in the C57/BL6 background. These approaches have extended the viability of the mutants up to postnatal day 0 and the adult stage, respectively, allowing us to delineate the important ciliary functions of *Rab23* during late developmental and adult stages.

In these mutant mice, our results indicate that *Rab23* plays a pivotal ciliary function in the neocortical region but not in the hippocampal neurons. A notable decrease in ciliation prevalence was observed in both the Tbr1-expressing postmitotic neurons of the neocortex at late embryonic stages and in the NeuN-expressing mature neocortical projection neurons at adult stages. These findings unveil a previously underappreciated function of *Rab23* in the adult central nervous system. Consistent with this finding, neurological-associated disorders such as intellectual disability and schizophrenia have been reported in cases of Carpenter syndrome [7,12,37]. Our earlier work also revealed the requirement of *Rab23* in modulating the migration of neocortical projection neurons during embryonic brain development [38]. Given these apparent correlations, further investigations to understand the molecular and cellular roles of Rab23 in neuronal development and neuronal pathophysiology are warranted.

In a similar vein, a previous study in the zebrafish model showed that morpholino-induced *rab23* knockdown morphants exhibited morphologically normal cilia in Kupffer's vesicle at the 8-somite stage, albeit with disrupted left-right patterning [36]. In our current investigation, we delved deeper to examine primary cilia in several tissue regions of *rab23* zebrafish morphants at a later embryonic stage, specifically at 24 hours post-fertilization. Our findings revealed a significant disturbances in the cilia quantity, with reduced acetylated-α-tubulin+ primary cilia on neural progenitor cells and motile cilia on ependymal cells, both lining the ventricular lumen of the forebrain neural tube. Conversely, cilia in other regions such as the pronephric duct and spinal cord neural tube appeared normal and were indistinguishable from the control counterpart.

We further demonstrate that Rab23 exerts GDP/GTP-binding dependent regulation of the Hedgehog signaling pathway in the neural progenitor cells. Compared to the control and the wild-type Rab23 overexpression group, the neural progenitor cells overexpressing the GTP-bound constitutively active form of Rab23 exhibit further inactivation of the Hh signaling pathway, whereas overexpression of the GDP-bound constitutively inactive mutant of Rab23 leads to the ectopic activation of the Hh signaling pathway. These results indicate that the classical Rab GTPase properties of Rab23, including its guanine nucleotide exchange factor (GEF) and the GTPase-activating protein (GAP)-dependent on/off actions, are essential for dynamically modulating the Hh signaling pathway in neural progenitor cells.

Strikingly, the variable and relatively mild primary cilia abnormalities in our *Rab23*-KO mutants differ markedly from the severe ciliogenesis defects observed in the Rab23's GEF complex mutants, Inturned-/- and Fuzzy-/- [39,40], which lack functional Rab23 GEF complexes. This phenotypic discrepancy potentially suggests that Intu/Fuz regulate ciliary functions through mechanisms that extend beyond their GEF activity toward Rab23. These observations imply that Intu/Fuz complexes likely possess Rab23-independent roles in ciliogenesis. Furthermore, Intu and Fuz have been demonstrated to modulate Hedgehog (Hh) signaling, with loss-of-function mutants showing downregulated pathway activity – a trend opposite to that caused by *Rab23* deletion [39,40]. This functional antagonism further supports the existence of Rab23-independent mechanisms through which Intu/Fuz regulate Hh signaling.

Interestingly, our data in cortical NPCs reveals opposing trends between cilia morphology and Hh signaling activity following the overexpression of Rab23 active and inactive mutants. Rab23 activation with the constitutively active Rab23QL expression elongates cilia length while inhibiting Hh signaling pathway. In contrary, inactive Rab23SN reduces cilia prevalence and produces shorter cilia, yet elevates the Hh pathway activity compared to controls. Given that loss of primary cilia typically impedes Hh pathway activation [41], yet this is not the case in the *Rab23*-deficient cells, in which the Hh signaling pathway is elevated despite disrupted ciliation. Given that previous work has demonstrated that Rab23 negatively affects Hh signaling pathway by binding to Suppressor-of-fused (SUFU) to prevent nuclear translocation of Gli1 transcription factor, a cilia-independent process [42]. We hypothesise that a similar mechanism could possibly explain the current observations in the mouse NPCs. Specifically, Rab23 may inhibit the Hh signaling pathway by acting on Gli1 transcription factor at the cytoplasmic level, independently of primary cilium. Nonetheless, this propose mechanism warrants further investigation.

Consistent with our previous findings in *Rab23*-KO granule cell precursors, where we demonstrated that Rab23 promotes SAG-induced Smoothened localization to the ciliary axoneme, revealing a cilia-dependent mechanism of action [18], our current findings demonstrate that Rab23 exerts multi-dimensional regulatory effects on Hedgehog signaling activity in NPCs. It positively influences the pathway through promoting primary cilia-dependent Smo-mediated Hh signal transduction. This is demonstrated by the finding that *Rab23* loss-of-function both prevents ligand-dependent Hh pathway activation and impairs ciliogenesis (Fig 6A–6E). Additionally, Rab23 also negatively affects Hh signaling activity, potentially by influencing Gli transcription factors in the cytoplasm through impeding the nuclear translocation of Gli1 [42]. This is further evidenced in our current work, whereby the active form Rab23QL expression suppresses Hh signaling pathway despite normal primary cilium prevalence, and in contrast, Rab23 deficiency causes over-activation of Hh signaling pathway (Fig 6C, 6D, 6F and 6G). This further indicates that different tissues and cell types may respond differently to the loss of Rab23 in terms of Hedgehog signaling activity, whereby Rab23-ablated cells without primary cilia may show partial activation of Hedgehog signaling due to the diminished primary cilia-dependent signaling response, whereas those with intact primary cilia may exhibit ectopic activation of the pathway. These findings suggest that Rab23 plays critical roles in modulating a context-dependent differential regulation of Hedgehog signaling pathway.

It's worthy to note that Carpenter syndrome presents a distinct phenotypic spectrum compared to other ciliopathies such as Joubert syndrome, Bardet-Biedl syndrome and AlstrÖm syndrome. Based on our data, it's plausible that this unique phenotypic spectrum may be attributed to the context-specific ciliary roles of Rab23, as well as the ciliary-independent regulatory functions of Rab23 on cell migration and other developmental signalling pathway such as the FGF, ERK and nodal signaling pathways [23,36,38]. For instance, it was reported that Rab23 influences FGFR and ERK1/2 signaling pathways in osteogenesis [23].

Our comprehensive *in vitro* and *in vivo* evidence strongly suggests that *RAB23* plays instrumental roles in ciliary function, thus positioning *RAB23* as part of the family of ciliary genes. Collectively, our findings provide new insights into the pathological mechanisms of Carpenter syndrome and pave the way for future development of clinical interventions. Additionally, the mouse mutants represent a valuable animal model for further investigations into the disease mechanism of Carpenter syndrome. Continued research in this area is imperative to advance our understanding and improve the clinical management of debilitating ciliopathy disorders.

Materials and methods

Animal and ethics approval

All animal protocols followed animal handling guideline approved by Hong Kong Baptist University Institutional Research Ethics Committee, the Department of Health, Hong Kong, as well as SingHealth Institutional Animal Care and Use Committee (IACUC), Singapore. The *Rab23-flox* mouse described in our previous work [18], was generated by Ozgene Pty Ltd. Nestin-Cre (The Jackson Laboratory cat. no. 003771) was a kind gift from Shawn Je H.S. from Duke-NUS Medical School. β-actin-Cre driver line was purchased from The Jackson Laboratory. Mice were housed in the animal facility, Department of Chemistry, HKBU, and the Specific Pathogen Free (SPF) animal facility at Duke-NUS Medical School, Singapore. The animal experiments described in this project included unbiased data from both female and male mice unless otherwise specified. The control animals were heterozygous $Rab23^{f/+}$ or homozygous $Rab23^{f/f}$ mutants.

Ethical approval for human clinical samples

Written consent was obtained from the parents of the Carpenter syndrome patient before the collection of the skin fibroblast sample for this study. IRB approval was provided by Central Oxford Research Ethics Committee, ref. C02.143, study name '*Genetic basis of craniofacial malformations'.* Studies conducted on the same Carpenter syndrome patient were previously reported in Jenkins et al 2007 [9] and Perlyn & Marsh 2008 [43].

Cryosection and immunohistochemistry

The cryosection and immunohistochemistry staining protocols have been reported in our previous work [18]. In brief, immediately post-perfusion, adult mouse brain samples were dissected from the skull and post-fixed in 4% paraformaldehyde for 2 hours on ice. For embryonic mouse samples, tissues of interest were dissected in ice-cold phosphate-buffered saline (PBS) immediately upon decapitation, transferred to 4% paraformaldehyde and incubated for 1–4 hours on ice for fixation. Fixed samples were transferred to 30% sucrose in phosphate buffer and stored at 4°C until subjected to cryosection. Tissue samples were sliced at 20 μm thickness and mounted on Superfrost glass slides. For immunohistochemistry staining, samples were subject to microwave heated antigen retrieval, 1 hour blocking in blocking buffer (1% bovine serum albumin (BSA), 2% donkey serum and 0.3% Tx-100) at room temperature, and primary antibody incubation at 4°C overnight. On the next day, samples were subjected to 3 times of PBS washing for 15 minutes each, followed by secondary antibody incubation for 2 hours at room temperature. Post-incubation, samples were washed 3 times with PBS for 15 minutes in each wash and mounted with home-made mounting media in semi-air-dry conditions. The primary antibodies and dilution factors used were: anti-rabbit Arl13b (Proteintech, 17711–1-AP 1:1500), anti-mouse Arl13b (DSHB/NeuroMAB clone N295B/66 1:800), anti-rabbit AC3 (Santa Cruz discontinued 1:1500), anti-mouse Nestin (Sigma/Millipore MAB5326 1:1000), anti-mouse Map2 (Sigma, M9942 1:1000), anti-rabbit Pax6 (Biolegend/Covance, PRV-278P 1:1000), anti-mouse NeuN (Sigma/Millipore, MAB377 1:800), anti-rabbit Tbr1 (Abcam, AB31940 1:500), anti-mouse acetylated alpha tubulin (Sigma Aldrich, T6793 1:2000). Secondary antibodies were from Invitrogen Life Technologies, Alexa Fluor, used at 1:1000 diluted in blocking buffer. Confocal images were captured by Nikon Confocal and Carl Zeiss LSM 710 confocal microscope.

Reprograming of human fibroblast to iPSCs

The human fibroblast reprogramming protocol was adapted from Okita *et. al.* [44] and described previously [45,46]. Briefly, human patient dermal fibroblasts were co-electroporated with episomal vectors (pCXLE-hOCT3/4, shp53, pCXLE-hSK, pCXLE-hUL) at 1 µg each. Electroporated cells were immediately seeded on Matrigel (BD Biosciences #354277)-coated 6 well plates and refreshed with mTeSR1 (Stem Cell Technologies) medium daily for approximately one month until the iPSC colonies reached the optimal size. At optimal size, the colonies were isolated, expanded, and characterised for normal karyotype and pluripotency through immunostaining examination of stem cells markers expression, including NANOG, TRA-1–60, OCT3/4 and SSEA4. The karyotyping and iPSCs characterisation for healthy control iPSCs were described previously [45,46]. Primary cilia analyses were performed within passage number (P) P5-P18.

Human NPC induction and neuron differentiation from iPSCs

The human NPC induction protocol was modified from Li *et. al.* [47] and Su *et. al.* [45]. Briefly, iPSCs at passage number P5 to P18 were seeded to 20% confluency, and cultured in NPC induction media (same as that used in Su et al., 2015, see below) for 7 days, which was replaced with fresh media every other day. On day 7, the culture was ready for passage and expansion into a 20 µg/ml PDL (Sigma Aldrich #P0899) and Matrigel (BD Biosciences #354277)-coated dish. Subsequently, the NPC culture was maintained in NPC maintenance media. Composition of hNPC induction medium; DMEMF12/Neurobasal medium at 1:1 ratio with 1x N2 Supplement, 1x B27 Supplement, 1x GlutaMax, 1x Penicillin/Streptomycin, 5 µg/ml BSA, 10 ng/ml human LIF, 4 µM CHIR99021 (GSK-3 inhibitor), 3 µM SB431542-TGF beta receptor inhibitor, and 0.1 µM Compound E, a γ-Secretase Inhibitor XXI. Composition of hNPC maintenance medium: DMEMF12/Neurobasal medium at 1:1 ratio with 1x N2 Supplement, 1x B27 Supplement, 1x GlutaMax, 1x Penicillin/Streptomycin, 5 µg/ml BSA, 10 ng/ml human LIF, 3 µM CHIR99021 (GSK-3 inhibitor), 2 µM SB431542-TGF beta receptor inhibitor.

For the neuronal differentiation, NPCs were seeded at 5 x 10^3 cells/cm^2 in 20 µg/ml PDL (Sigma Aldrich #P6407) and Matrigel coated coverslips in 24 well plate with neuronal differentiation medium (1x N2 Supplement (Life Technologies #17502048), 1x L-Glutamine (Life Technologies #25030081), 1x Pen/Strep (Life Technologies #15140122) in DMEMF12/Neurobasal (Life Technologies #21103049) medium mixture at 1:1 ratio), with. 10 µM of Rho-associated protein kinase (ROCK) inhibitor (Y-27632, ATGG) freshly added. One-half of the media was gently refreshed without ROCK inhibitor every 2–3 days. MAP2-expressing differentiated neurons were obtained on day 18–28. The primary cilia on MAP2-expressing neurons were examined at day 18 and 21 post-differentiation.

Mouse neural progenitor cell culture and Smoothened agonist (SAG) stimulation

Postnatal day 0 cerebral cortical tissues were dissected and digested in digestion buffer consisting of Earle's Balanced Salt Solution (EBSS) containing Papain (Worthington LS003126) diluted at 1000x, 0.1 mg/ml DNaseI (Roche catalog #11284932001), 5.5 mM cysteine-HCl, incubated for 30 minutes at 37°C. The digested tissues were then resuspended and dissociated into single cells suspension by gentle pipetting with a P1000 pipettor in DMEM/F-12 medium. The cell suspension was passed through a 70-µm cell strainer (SPL catalog #93070) and centrifuged at 1,200 rpm for 5 minutes. The cell pellets were then resuspended and cultured in DMEM/F12 maintenance medium containing 20 ng/ml FGF, 20 ng/ml EGF, 2 µg/ml Heparin, 1% N2 Supplement (Life Technologies, catalog #17502048) and 1% penicillin/streptomycin.

The cells were cultured on a non-adherent surface for 5–7 days to allow neurosphere formation. When the neurospheres reached a diameter of 120–150 μm, the medium with neurospheres was transferred to a conical centrifuge tube and centrifuged at 1,000 rpm for 5 minutes. The neurospheres were incubated in Accutase for 5 minutes, and then maintenance medium was added to terminate the enzyme activity and dissociate the neurospheres into a single-cell suspension. Dissociated NPCs were plated on 20 μg/ml poly-D-lysine (Sigma-Aldrich, catalog #P0899)-coated culture plates. Smoothened agonist (SAG) stimulation was performed as previously reported [18]. Briefly, the NPCs were seeded at equal cell density at 3×10^4 per well on a 96-well plate and infected by lentivirus carrying a 7Gli:GFP reporter construct (Addgene #110494; Li et al., 2016) [49]. On day 4 post-infection, 0.2 μM SAG (Cayman Chemical, catalog #11914–1) was added to the culture and incubated for 24 hours. Green fluorescence reporter signals were measured by fluorescence microplate reader 24 hours post-treatment. For the control group, an equal volume of dimethyl sulfoxide (DMSO) was added as the negative control to drug treatment.

Mouse primary cortical neuron culture

Primary cortical neurons culture protocol was described previously [38]. In brief, primary cortical neurons were isolated from postnatal day 0 mice. The cortical region was microdissected in ice-cold Earle's Balanced Salt Solution (EBSS) and digested in enzymatic solution containing EBSS with 1000 × diluted papain (Worthington #LS003126), 0.1 mg/ml DNase I (Roche #11284932001), and 5.5 mM cysteine-HCl. Tissues were incubated in digestion buffer for 30 minutes at 37°C with gentle agitation. Following enzymatic digestion, tissues were mechanically dissociated into single-cell suspensions by gentle trituration using a P1000 pipette in DMEM/F-12 medium. The cell suspension was filtered through a 70-μm cell strainer (SPL #93070) to remove undigested tissue fragments and centrifuged at 1,200 rpm for 5 minutes. The resulting cell pellet was resuspended in complete neuronal culture medium consisting of Neurobasal medium supplemented with 0.5% glucose, 0.4 mM L-glutamine, and 2% B27 supplement. Cells were plated on 40 μg/ml poly-D-lysine and Matrigel coated culture plate and maintained at 37°C in a humidified 5% CO2 incubator. For optimal cell health, half of the culture medium was replaced with fresh medium every other day.

Mouse embryonic fibroblasts (MEFs) culture

Primary mouse embryonic fibroblasts were isolated from embryonic day 13.5 (E13.5) mouse embryos. Following euthanasia of the pregnant dam, embryos were dissected in PBS. Internal organs were removed. The remaining embryonic tissues were minced into smaller fragments using a sterile forcep. Tissues were incubated in the 0.05% trypsin-EDTA solution at 37°C for 20 minutes with gentle agitation. Following enzymatic digestion, tissues were mechanically dissociated into single-cell suspensions by gentle trituration using a P1000 pipette in DMEM medium. Isolated MEFs were plated in tissue culture-treated dish and maintained at 37°C in a humidified 5% CO_2 atmosphere. Cells were typically passaged at 70–80% confluence using 0.05% trypsin-EDTA and utilized for experiments between passages 2–15.

Lentivirus packaging and production

The lentiviruses used for the overexpression of full-length Rab23 and its mutant forms in the mouse NPCs were produced using HEK293GP packaging cells (Takara) co-transfected with VSV-G, delta8.9, together with FUGW-GFP as the lentiviral vector carrying the Rab23WT, Rab23S23N, and Rab23Q68L, respectively. To harvest the viruses, the culture media was collected 24 hours post-transfection, concentrated through standard ultra-centrifugation methods, and store in aliquots at -80 °C. The FUGW constructs inserted with the Rab23 full-length and the mutant forms used were described in our previous work [18]. In brief, Rab23S23N is the constitutive negative mutant, whereas Rab23Q68L is the GTP-bound constitutive active mutant.

Real-time qPCR

Total RNA was extracted using Trizol (Vazyme). cDNA was reverse transcribed from equal amounts of RNA using the iScript cDNA Synthesis Kit (Biorad). Using equal volumes of cDNA as the PCR template, the corresponding gene expression levels were evaluated by quantitative real-time PCR (qPCR) using a TB Green Master Mix (Takara). PCR primers used were:

Gapdh: F-5′-TTCACCACCATGGAGAAGGC-3′,

R-5′-GGCATGGACTGTGGTCATGA-3′;

Rab23: F-5′-AGGCCTACTATCGAGGAGCC-3′,

R-5′-TTAGCCTTTTGGCCAGTCCC-3′;

Gli1: F-5′-CCCATAGGGTCTCGGGGTCTCAAAC-3′,

R-5′-GGAGGACCTGCGGCTGACTGTGTAA-3′;

Ki67: F-5′-CATTGACCGCTCCTTTAGGTATGAAG-3′,

R-5′-TTGGTATCTTGACCTTCCCCATCAG-3′;

Sox2: F-5′-ACAGATGCAACCGATGCACC-3′,

R-5′-TGGAGTTGTACTGCAGGGCG-3′;

Nestin: F-5′-CGCTGGAACAGAGATTGGAAG-3′,

R-5′-CATCTTGAGGTGTGCCAGTT-3′;

Shh: F-5′-CCGGCTTCGACTGGGTGTACTA-3′,

R-5′-CGCCACCGAGTTCTCTGCTT-3′.

Immunocytochemistry

Cells cultured on coverslips were fixed with 4% paraformaldehyde for 10 minutes at room temperature. Subsequently, the cells were washed with 1 x PBS and permeabilized with 0.1% Triton X-100 for 15 minutes and blocked in a blocking solution of 1% BSA in PBS for 1 hour at room temperature. The cells were then subjected to overnight incubation at 4°C with primary antibodies diluted in the blocking solution. Primary antibodies used were: mouse anti-Nestin (1:1000, Santa Cruz Biotechnology), rabbit anti-Arl13b (1:1000, Proteintech), mouse anti-OCT3/4 (1:500 Santa Cruz Biotechnology), rabbit anti-NANOG (1:100, Cell Signaling Technollogy), mouse anti-SSEA4 (1:500, Milliporer), mouse anti-TRA-1–60 (1:100, Santa Cruz Biotechnology), goat anti-SOX2 (1:500 Santa Cruz Biotechnology). After three washes with PBS, the cells were incubated with fluorophore-conjugated secondary antibodies (Alexa Fluor, Life Technologies) for 1 hour at room temperature. Following three additional PBS washes, the cells were mounted in homemade mounting media, kept in dark and air-dry before proceeding to confocal imaging.

Injection of zebrafish

Wild-type zebrafish of the AB strain were maintained under standard conditions of fish husbandry. Freshly fertilized zebrafish eggs were injected with mRNA (100 ng/µl) and *rab23* morpholino (600 µM) at the one- to two-cell stage in a volume of approximately 1 µl. Approximately 200 embryos were injected for morpholino knockdown or mRNA rescue. The injected embryos were cultured at 28°C, and embryos were harvested at respective timepoints for RT-PCR (Qiagen) or fixed at specific developmental stages for further analysis. Morpholinos were purchased from GeneTools. A splice-blocking morpholino (5′- GTAAAATCTCGCTCACATGATCTGC -3′) was selected for knocking down *Rab23*. This splice-blocking MO, which allows the efficiency of MO inhibition to be determined through PCR, was used for all the rab23 morphants shown here. The control morpholino (5′-CCTCTTACCTCAGTTACAATTTATA-3′) used was the scrambled sequence from Gene Tools.

Whole-mount antibody staining

Whole-mount antibody staining on zebrafish embryos was performed according to standard protocols. Monoclonal anti-acetylated-α-tubulin (1:500; Sigma Aldrich) was used to stain cilia. For confocal microscopy, appropriate Alexa-Fluor conjugated secondary antibody was used for signal detection and embryos were counterstained with 4,6-diamidino-2-phenylindole (DAPI) to visualize cell nuclei. Stained embryos were dissected from their yolk and mounted in 70% glycerol. High-resolution images of embryos were captured using a Zeiss LSM 710 confocal microscope (Carl Zeiss Pte Ltd, Singapore).

Cloning and *in vitro* transcription of capped mRNA

cDNA was synthesized from 24 hours post-fertilization (hpf) wild-type embryos using a cDNA synthesis kit (Invitrogen). The cDNA template was used for PCR amplification of the full-length zebrafish *rab23*. The PCR products were cloned into TOPO vector and subsequently sub-cloned into pCS2-GFPxlt for the rescue experiment. Plasmid encoding *rab23* was linearized, and capped, full-length mRNA was transcribed from this template using the mMessage mMachine Kit (Ambion). The mRNA was injected into one- to two-cell stage embryos in combination with a morpholino.

Primary cilia length analysis

For the *in vivo* tissue samples, the measurements of cilia length were performed on 3D maximum intensity projection of z-stacked confocal images (at 15–20 μm thickness of z-layers captured at 0.5 μm intervals) taken from 2-3 spatially matched tissue slices from each embryo, with 3–4 biological replicates in each genotype. For the *in vitro* samples, the measurement of cilia length was performed on 3D projected confocal images (at 10–15 μm thickness of z-layers captured at 0.5 μm intervals) taken from 2-3 random views in each group, captured with 60x objective, scanning and saved at 1024x1024 pixel size. The box plots illustrate data from 3 - 5 independent experiments.

The analyses of cilia length were performed on 3D projected images using the ImageJ plugin CiliaQ [48] and Nikon NIS-Elements Advance Research (AR) imaging software. For analyses using CiliaQ, the default parameters for 3D CANNY-threshold for ciliary reconstruction was applied. Background signal subtraction was applied to animal tissue slices and human NPCs images prior to analysis. In the measurement of cilia length, the data points at below 0.2 μm and above 8 μm were excluded as potential false signals. For analysis using NIS-Elements AR software, General Analysis 3 (GA3) program was used to analyse the cilia length after refining the binary parameter, The lower threshold was set at > 0.2 μm. All data analysis was conducted using at least 3 biological replicates in each genotype.

Statistical analysis

Unpaired 2-tailed Student's t-test was performed for statistical comparison between two groups. For comparison of more than two groups, one-way ANOVA, Bonferroni's Multiple Comparison Test was used. Error bars depict SEM (standard error of the mean). P value: **** $p \leq 0.0001$, *** $p \leq 0.001$, ** $p \leq 0.01$, * $p \leq 0.05$. Graphs with boxplots depict the interquartile range of the ciliary length, with the lower quartile (Q1) representing the 25th percentile of the data, and the upper quartile (Q3) representing the 75th percentile of the data. The line inside the box indicates the median of the data. For *in vivo* tissue sections analyses on Z-projected confocal images, 3–4 confocal images spanning the upper and lower Z-planes of the comparable region of interest were captured with the same imaging parameters, and analysed to represent the result for each animal. In general, 3–4 animals were analysed for each genotype, unless stated otherwise. For cell culture experiments, all statistical results were collected from at least 3–5 independent cultures. For the quantification of percentage of ciliation in human NPCs and fibroblast, we performed blinded data analyses for these two cell types.

Supporting information

S1 Fig. Amino acid sequence alignment reveals highly conserved RAB23 protein across different vertebrates. Multiple protein sequence alignment of RAB23 in zebrafish (*Danio rerio*), mouse (*Mus musculus*), rhesus macaque (*Macaca mulatta*) and humans (*Homo sapiens*). The sequences highlighted in dark blue depict the identical amino acid regions. *Danio rerio* shares 84.39% identity with human RAB23. *Mus musculus* shares 93.25% identity with human.
(TIF)

S2 Fig. A portion of Actin-CKO mutant displays more severe brain deformity. Representative images show morphological appearance of control and actin-CKO mutant mice at E18.5, illustrating actin-CKO mutant mice that display relatively severe brain deformity.
(TIF)

S3 Fig. *rab23* morphants exhibit slightly but significantly larger head size. Graph representing quantitative head size measurement between control and *rab23* morphant at 72 hpf. The head size was determined by measuring the distance between the eyes in the dorsal view images. The average head size of morphants was slightly yet significantly larger than the control group. n = 12 for each group ** *P* value $\leq$ 0.01 Unpaired Student's t-test. Error bars depict S.D.
(TIF)

S4 Fig. Loss of *Rab23* decreases ciliation in MEFs and Tbr1 + intermediate progenitors. (A-B) Representative immunohistochemistry images (low power on left, magnification of boxed region on right) and **(B)** graph depicting quantification of the proportion of Acetylated-α-tubulin+ primary cilia against Tbr1+ (green) neocortical layer VI neurons in the neocortex at E18.5. A significant two-fold reduction in the number of primary cilia is observed in the cerebral cortex of actin-CKO mouse embryos. Each dot represents the average percentage count across three brain sections per animal. n = 4 per group. * *P* value ≤ 0.05, Unpaired Student's t-test. **(C)** Representative immunocytochemistry images depicting the Arl13b+ and Acetylated-α-tubulin+ primary cilia in the mouse embryonic fibroblasts cultured from E13.5 control and actin-CKO respectively.
(TIF)

S5 Fig. Carpenter syndrome patient-derived iPSCs display shorter primary cilia. Representative immunocytochemistry images depicting the primary cilia of healthy adult and Carpenter syndrome patient iPSCs co-immunostained for ARL13B and ACETYLATED-α-TUBULIN respectively.
(TIF)

S1 Data. The numerical data for the graphs shown in Fig 1.
(XLSX)

S2 Data. The numerical data for the graphs shown in Fig 2.
(XLSX)

S3 Data. The numerical data for the graphs shown in Fig 3.
(XLSX)

S4 Data. The numerical data for the graphs shown in Fig 4.
(XLSX)

S5 Data. The numerical data for the graphs shown in Fig 5.
(XLSX)

S6 Data. The numerical data for the graphs shown in Fig 6.
(XLSX)

Acknowledgments

We thank Professor Bor Luen Tang from the National University of Singapore for the constructive discussions and comments on this work. We thank Dr. Eyleen LK Goh for supporting some of the experimental reagents. We thank Wee Lin Wong and Cho Wai Lo for the assistance on figure editing and some data analysis. We thank Lam Sheung Yuen and Chui Wai Hui for the assistance on data analysis.

Author contributions

Conceptualization: Catherine Hong Huan Hor.

Formal analysis: Wan Ying Leong, Wai Lam Tung, Catherine Hong Huan Hor.

Funding acquisition: Catherine Hong Huan Hor.

Investigation: Wan Ying Leong, Wai Lam Tung, Catherine Hong Huan Hor.

Methodology: Wan Ying Leong.

Project administration: Catherine Hong Huan Hor.

Resources: Andrew O M Wilkie, Catherine Hong Huan Hor.

Supervision: Catherine Hong Huan Hor.

Visualization: Wan Ying Leong, Wai Lam Tung, Catherine Hong Huan Hor.

Writing – original draft: Wan Ying Leong, Catherine Hong Huan Hor.

Writing – review & editing: Wai Lam Tung, Andrew O M Wilkie, Catherine Hong Huan Hor.

References

1. Wheway G, Nazlamova L, Hancock JT. Signaling through the Primary Cilium. Front Cell Dev Biol. 2018;6:8. https://doi.org/10.3389/fcell.2018.00008 PMID: 29473038
2. Gerdes JM, Davis EE, Katsanis N. The vertebrate primary cilium in development, homeostasis, and disease. Cell. 2009;137(1):32–45. https://doi.org/10.1016/j.cell.2009.03.023 PMID: 19345185
3. Silva DF, Cavadas C. Primary cilia shape hallmarks of health and aging. Trends Mol Med. 2023;29(7):567–79. https://doi.org/10.1016/j.molmed.2023.04.001 PMID: 37137787
4. Reiter JF, Leroux MR. Genes and molecular pathways underpinning ciliopathies. Nat Rev Mol Cell Biol. 2017;18(9):533–47. https://doi.org/10.1038/nrm.2017.60 PMID: 28698599
5. Waters AM, Beales PL. Ciliopathies: an expanding disease spectrum. Pediatr Nephrol. 2011;26(7):1039–56. https://doi.org/10.1007/s00467-010-1731-7 PMID: 21210154
6. Haye D, Collet C, Sembely-Taveau C, Haddad G, Denis C, Soulé N, et al. Prenatal findings in carpenter syndrome and a novel mutation in RAB23. Am J Med Genet. 2014;164A:2926–30.
7. Alessandri J-L, Dagoneau N, Laville J-M, Baruteau J, Hébert J-C, Cormier-Daire V. RAB23 mutation in a large family from Comoros Islands with Carpenter syndrome. Am J Med Genet A. 2010;152A(4):982–6. https://doi.org/10.1002/ajmg.a.33327 PMID: 20358613
8. Jenkins D, Baynam G, De Catte L, Elcioglu N, Gabbett MT, Hudgins L, et al. Carpenter syndrome: extended RAB23 mutation spectrum and analysis of nonsense-mediated mRNA decay. Hum Mutat. 2011;32(4):E2069-78. https://doi.org/10.1002/humu.21457 PMID: 21412941
9. Jenkins D, Seelow D, Jehee FS, Perlyn CA, Alonso LG, Bueno DF, et al. RAB23 mutations in Carpenter syndrome imply an unexpected role for hedgehog signaling in cranial-suture development and obesity. Am J Hum Genet. 2007;80(6):1162–70. https://doi.org/10.1086/518047 PMID: 17503333

10. Tarhan E, Oğuz H, Safak MA, Samim E. The Carpenter syndrome phenotype. Int J Pediatr Otorhinolaryngol. 2004;68(3):353–7. https://doi.org/10.1016/j.ijporl.2003.10.009 PMID: 15129947

11. Hidestrand P, Vasconez H, Cottrill C. Carpenter syndrome. J Craniofac Surg. 2009;20:254–6.

12. Lodhia J, Rego-Garcia I, Koipapi S, Sadiq A, Msuya D, Spaendonk R, et al. Carpenter syndrome in a patient from Tanzania. Am J Med Genet A. 2021;185(3):986–9. https://doi.org/10.1002/ajmg.a.62015 PMID: 33368989

13. Kadakia S, Helman SN, Healy NJ, Saman M, Wood-Smith D. Carpenter syndrome: a review for the craniofacial surgeon. J Craniofac Surg. 2014;25(5):1653–7. https://doi.org/10.1097/SCS.0000000000001121 PMID: 25162549

14. Zhao H, Khan Z, Westlake CJ. Ciliogenesis membrane dynamics and organization. Semin Cell Dev Biol. 2023;133:20–31. https://doi.org/10.1016/j.semcdb.2022.03.021 PMID: 35351373

15. Gerondopoulos A, Strutt H, Stevenson NL, Sobajima T, Levine TP, Stephens DJ, et al. Planar cell polarity effector proteins inturned and fuzzy form a Rab23 GEF complex. Curr Biol. 2019;29(19):3323-3330.e8. https://doi.org/10.1016/j.cub.2019.07.090 PMID: 31564489

16. Eggenschwiler JT, Espinoza E, Anderson KV. Rab23 is an essential negative regulator of the mouse Sonic hedgehog signalling pathway. Nature. 2001;412(6843):194–8. https://doi.org/10.1038/35084089 PMID: 11449277

17. Denef N, Neubüser D, Perez L, Cohen SM. Hedgehog induces opposite changes in turnover and subcellular localization of patched and smoothened. Cell. 2000;102(4):521–31. https://doi.org/10.1016/s0092-8674(00)00056-8 PMID: 10966113

18. Hor CHH, Lo JCW, Cham ALS, Leong WY, Goh ELK. Multifaceted functions of Rab23 on primary cilium-mediated and hedgehog signaling-mediated cerebellar granule cell proliferation. J Neurosci. 2021;41(32):6850–63. https://doi.org/10.1523/JNEUROSCI.3005-20.2021 PMID: 34210780

19. Leaf A, Von Zastrow M. Dopamine receptors reveal an essential role of IFT-B, KIF17, and Rab23 in delivering specific receptors to primary cilia. Elife. 2015;4.

20. Lim YS, Tang BL. A role for Rab23 in the trafficking of Kif17 to the primary cilium. J Cell Sci. 2015;128:2996–3008.

21. Boehlke C, Bashkurov M, Buescher A, Krick T, John A-K, Nitschke R, et al. Differential role of Rab proteins in ciliary trafficking: Rab23 regulates smoothened levels. J Cell Sci. 2010;123(Pt 9):1460–7. https://doi.org/10.1242/jcs.058883 PMID: 20375059

22. Yoshimura S-I, Egerer J, Fuchs E, Haas AK, Barr FA. Functional dissection of Rab GTPases involved in primary cilium formation. J Cell Biol. 2007;178(3):363–9. https://doi.org/10.1083/jcb.200703047 PMID: 17646400

23. Hasan MR, Takatalo M, Ma H, Rice R, Mustonen T, Rice DP. RAB23 coordinates early osteogenesis by repressing FGF10-pERK1/2 and GLI1. Elife. 2020;9.

24. Damerla RR, Cui C, Gabriel GC, Liu X, Craige B, Gibbs BC. Novel Jbts17 mutant mouse model of Joubert syndrome with cilia transition zone defects and cerebellar and other ciliopathy related anomalies. Hum Mol Genet. 2015;24(14):3994.

25. Youn YH, Han YG. Primary cilia in brain development and diseases. Am J Pathol. 2018;188(1):11–22.

26. Oud M, Lamers I, Arts H. Ciliopathies: genetics in pediatric medicine. J Pediatr Genet. 2016;6(01):018–29.

27. Guemez-Gamboa A, Coufal NG, Gleeson JG. Primary cilia in the developing and mature brain. Neuron. 2014;82(3):511–21. https://doi.org/10.1016/j.neuron.2014.04.024 PMID: 24811376

28. Wallmeier J, Frank D, Shoemark A, Nöthe-Menchen T, Cindric S, Olbrich H, et al. De novo mutations in FOXJ1 result in a motile ciliopathy with hydrocephalus and randomization of left/right body asymmetry. Am J Hum Genet. 2019;105(5):1030–9. https://doi.org/10.1016/j.ajhg.2019.09.022 PMID: 31630787

29. Movva S, Kotecha UH, Sharma D, Puri RD, Verma IC. Prenatal diagnosis and elucidation of a novel molecular mechanism in Carpenter syndrome. J Fetal Med. 2014;01(02):89–93. https://doi.org/10.1007/s40556-014-0017-8

30. Begam M, Bekdache GN, Al Gazali L, Mirghani H. Prenatal diagnosis of Carpenter syndrome at 16 weeks: role of 3D ultrasound. Ultrasound Obstet Gynecol. 2011;38(S1):149.

31. Liu B, Chen S, Johnson C, Helms JA. A ciliopathy with hydrocephalus, isolated craniosynostosis, hypertelorism, and clefting caused by deletion of Kif3a. Reprod Toxicol. 2014;48:88–97. https://doi.org/10.1016/j.reprotox.2014.05.009 PMID: 24887031

32. Gerth-Kahlert C, Koller S. Retinale Ziliopathien. Klin Monbl Augenheilkd. 2018;235(3):264–72.

33. Badano JL, Mitsuma N, Beales PL, Katsanis N. The ciliopathies: an emerging class of human genetic disorders. Annu Rev Genomics Hum Genet. 2006;7:125–48. https://doi.org/10.1146/annurev.genom.7.080505.115610 PMID: 16722803

34. Ben-Salem S, Begum MA, Ali BR, Al-Gazali L. A novel aberrant splice site mutation in RAB23 leads to an eight nucleotide deletion in the mRNA and is responsible for carpenter syndrome in a consanguineous emirati family. Mol Syndromol. 2013;3:255–61.

35. Hor CH, Goh EL. Small GTPases in hedgehog signalling: emerging insights into the disease mechanisms of Rab23-mediated and Arl13b-mediated ciliopathies. Curr Opin Genet Dev. 2019;56:61–8.

36. Fuller K, O'Connell JT, Gordon J, Mauti O, Eggenschwiler J. Rab23 regulates Nodal signaling in vertebrate left-right patterning independently of the Hedgehog pathway. Dev Biol. 2014;391(2):182–95. https://doi.org/10.1016/j.ydbio.2014.04.012 PMID: 24780629

37. Bersani G, Maddalena F, Pasquini M, Orlandi V, Pancheri P. Association of schizophrenia and Carpenter syndrome. Acta Neuropsychiatr. 2003;15(5):304–5. https://doi.org/10.1034/j.1601-5215.2003.00046.x PMID: 26983661

38. Hor CHH, Goh ELK. Rab23 regulates radial migration of projection neurons via N-cadherin. Cerebral Cortex. 2018;28(4):1516–31.

39. Zeng H, Hoover AN, Liu A. PCP effector gene Inturned is an important regulator of cilia formation and embryonic development in mammals. Dev Biol. 2010;339(2):418–28. https://doi.org/10.1016/j.ydbio.2010.01.003 PMID: 20067783

40. Heydeck W, Zeng H, Liu A. Planar cell polarity effector gene Fuzzy regulates cilia formation and Hedgehog signal transduction in mouse. Dev Dyn. 2009;238(12):3035–42. https://doi.org/10.1002/dvdy.22130 PMID: 19877275

41. Singla V, Reiter JF. The primary cilium as the cell's antenna: signaling at a sensory organelle. Science. 2006;313(5787):629–33.

42. Chi S, Xie G, Liu H, Chen K, Zhang X, Li C, et al. Rab23 negatively regulates Gli1 transcriptional factor in a Su(Fu)-dependent manner. Cell Signal. 2012;24(6):1222–8. https://doi.org/10.1016/j.cellsig.2012.02.004 PMID: 22365972

43. Perlyn CA, Marsh JL. Craniofacial dysmorphology of Carpenter syndrome: lessons from three affected siblings. Plast Reconstr Surg. 2008;121(3):971–81. https://doi.org/10.1097/01.prs.0000299284.92862.6c PMID: 18317146

44. Okita K, Matsumura Y, Sato Y, Okada A, Morizane A, Okamoto S, et al. A more efficient method to generate integration-free human iPS cells. Nat Methods. 2011;8(5):409–12. https://doi.org/10.1038/nmeth.1591 PMID: 21460823

45. Su CTE, Yoon S-I, Marcy G, Chin EWM, Augustine GJ, Goh ELK. An optogenetic approach for assessing formation of neuronal connections in a co-culture system. JoVE. 2015;(96):e52408. https://doi.org/10.3791/52408-v

46. Chin EWM, Marcy G, Yoon SI, Ma D, Rosales FJ, Augustine GJ. Choline ameliorates disease phenotypes in human iPSC models of Rett syndrome. Neuromol Med. 2016;18(3):364–77.

47. Li W, Sun W, Zhang Y, Wei W, Ambasudhan R, Xia P, et al. Rapid induction and long-term self-renewal of primitive neural precursors from human embryonic stem cells by small molecule inhibitors. Proc Natl Acad Sci U S A. 2011;108(20):8299–304. https://doi.org/10.1073/pnas.1014041108 PMID: 21525408

48. Hansen JN, Rassmann S, Stüven B, Jurisch-Yaksi N, Wachten D. CiliaQ: a simple, open-source software for automated quantification of ciliary morphology and fluorescence in 2D, 3D, and 4D images. Eur Phys J E Soft Matter. 2021;44(2):18. https://doi.org/10.1140/epje/s10189-021-00031-y PMID: 33683488

49. Li T, Fan J, Blanco-Sánchez B, Giagtzoglou N, Lin G, Yamamoto S, et al. Ubr3, a novel modulator of hh signaling affects the degradation of costal-2 and Kif7 through poly-ubiquitination. PLoS Genet. 2016;12(5):e1006054. https://doi.org/10.1371/journal.pgen.1006054 PMID: 27195754